nature biomedical engineering

Article

https://doi.org/10.1038/s41551-025-01361-4

Osteopontin attenuates the foreign-body response to silicone implants

Received: 14 July 2023

Accepted: 28 January 2025

Published online: 24 March 2025

Check for updates

Michelle F. Griffin[1,5], Jennifer B. Parker[1,2,5], Ruth Tevlin[1], Norah E. Liang[1], Caleb Valencia[1,2], Annah Morgan[1], Maxwell Kuhnert[1], Mauricio Downer Jr.[1], Emily L. Meany[3], Jason L. Guo[1], Dominic Henn[1], Renato S. Navarro[4], Kerry Shefren[1], Dung Nguyen[1], Geoffrey C. Gurtner[1], Sarah C. Heilshorn[4], Charles K. F. Chan[1,2], Michael Januszyk[1], Eric A. Appel[4], Arash Momeni[1] ✉, Derrick C. Wan[1] ✉ & Michael T. Longaker[1,2] ✉

The inflammatory process resulting in the fibrotic encapsulation of implants has been well studied. However, how acellular dermal matrix (ADM) used in breast reconstruction elicits an attenuated foreign-body response (FBR) remains unclear. Here, by leveraging single-cell RNA-sequencing and proteomic data from pairs of fibrotically encapsulated specimens (bare silicone and silicone wrapped with ADM) collected from individuals undergoing breast reconstruction, we show that high levels of the extracellular-matrix protein osteopontin are associated with the use of ADM as a silicone wrapping. In mice with osteopontin knocked out, FBR attenuation by ADM-coated implants was abrogated. In wild-type mice, the sustained release of recombinant osteopontin from a hydrogel placed adjacent to a silicone implant attenuated the FBR in the absence of ADM. Our findings suggest strategies for the further minimization of the FBR.

The use of implantable biomedical devices increases exponentially each year, propelled by a combination of ever-advancing technological innovation and the clinical demands of an expanding senior population[1]. The implantable devices market was valued at approximately US$120 billion dollars (all $ symbols refer to US dollars hereafter) worldwide in 2021 and is estimated to rise to $168.3 billion dollars within the next 4 years[2]. Despite their notable potential for improving health and quality of life, all biological implants are limited by foreign-body response (FBR), an immune-mediated reaction involving chronic inflammation, foreign-body giant cell formation and ultimately fibrous encapsulation of foreign material[1–3]. Pathologic FBR can lead to implant malfunction, superimposed infection, soft-tissue disfigurement, and may ultimately necessitate reoperation procedures and material explant[4,5]. Recent studies over the past decade have gleaned some insights regarding the mechanistic underpinning of FBR. For example, mechanotransduction signalling pathways such as transforming growth factor beta (TGF-β) and transient receptor potential vanilloid 4 (TRPV4)-Ras-related C3 botulinum toxin substrate 1 (Rac1) have been shown to play roles in multinucleated giant cell formation and fibrosis[6–8]. Meanwhile, substantial work has also been conducted regarding the effect of implant material stiffness on the extent of FBR, with stiffer materials leading to increased fibrosis[8,9]. Furthermore, implant surface topography has been shown to alter the degree of inflammation during FBR. One study suggested that excess or absence of surface topography leads to increased surface T cell-mediated immune response[10]. With an increasing understanding of the mechanism underlying FBR, many groups currently focus on the development of strategies to minimize FBR, including the application of new biomaterials and coatings[11].

For example, acellular dermal matrix (ADM), a decellularized tissue often derived from cadaveric dermis with an intact extracellular matrix (ECM), is thought to attenuate FBR by providing a biomimetic scaffold for native tissue incorporation[12,13]. Animal models and human

[1]Department of Surgery, Division of Plastic and Reconstructive Surgery, Stanford University School of Medicine, Stanford, CA, USA. [2]Institute for Stem Cell Biology and Regenerative Medicine, Stanford University School of Medicine, Stanford, CA, USA. [3]Department of Bioengineering, Stanford University, Stanford, CA, USA. [4]Department of Materials Science and Engineering, Stanford University, Stanford, CA, USA. [5]These authors contributed equally: Michelle F. Griffin, Jennifer B. Parker. ✉e-mail: amomeni@stanford.edu; dwan@stanford.edu; longaker@stanford.edu

histopathologic studies suggest that rates of capsular contracture, the clinical term used for FBR, are lower in the presence of ADM because the material may reduce or delay capsule formation[14–19]. Other studies have shown that ADM downregulates inflammation[12]. However, the exact mechanism of action through which ADM modifies the periprosthetic FBR is not well understood. Rigorous molecular characterization of this phenomenon presents an opportunity to not only revolutionize prosthetic-based medicine, but also overcome the inevitable biologic process of FBR. More specifically, we hypothesize that application of ADM alters the implant microenvironment proximal to the implant. As ADM is an adjunct frequently used in breast reconstruction that is both expensive and in limited supply, a primary goal of this study is to determine how ADM specifically modulates FBR. With a deeper understanding of the biology underlying the mitigating effects of ADM, we hope to identify effective treatment strategies targeting this mechanism without the use of costly ADM.

First introduced to support the lower pole of the breast and improve aesthetic outcomes following implant-based breast reconstruction[20], subsequent clinical studies illustrated that ADM use was associated with decreased rates of capsular contracture[18,21–28]. For example, in a study of 1,584 ADM-assisted breast reconstruction procedures, less than 1% rate of capsular contracture was reported[29]. These results are clinically important as capsular contracture may often lead to pain, aesthetic changes and eventual revision procedures[30]. Since the 2000s, ADM use in implant-based breast reconstruction has grown in frequency. Despite limited understanding of the mechanism underlying decreased FBR with ADM application, it is estimated that ADM is utilized in over 60% of alloplastic reconstruction in the United States[31].

In this study, we undertake a mechanistic approach to investigate FBR in the context of ADM use. We use implant-based breast reconstruction as a model for understanding how ADM modulates FBR. Through analysis of paired patient-derived capsule specimens collected during breast reconstruction, we identify that ADM is biologically active, with significant differences seen in capsule architecture, microenvironment protein signalling and transcriptional activity in capsule tissue specimens adjacent to ADM ('ADM capsule') versus capsule tissue not exposed to ADM ('Native capsule'). Using multi-omic studies, we demonstrate that ADM promotes an attenuated FBR associated with activation of the *SPP1* gene in monocytes and macrophages. SPP1 is a protein expressed in a variety of tissues, including bone, kidney and brain[32]. It plays a key role in bone remodelling by enabling anchoring of osteoclasts[33]. In the immune system, SPP1 has also been shown to bind to a number of integrin receptors and provide function in cell adhesion and migration[34]. Outside of homeostasis, SPP1 has been shown to be implicated in multiple processes. Notably, it has been associated with pulmonary and liver fibrosis[35,36], as well as with both pro-fibrotic and anti-fibrotic outcomes in FBR[10,37,38]. SPP1 signalling has also been observed in different forms of cancer, including colon, head and neck, and lung[39]. Interestingly, this gene also shows promise as a driver for regeneration in certain tissues, such as muscle[40–42]. Therefore, its function is highly context dependent.

Given the complex and nuanced nature of SPP1 function, to further interrogate these findings, we developed an analogous mouse model of FBR, treated with and without ADM. Transcriptional analysis of mouse capsules validated findings of attenuated FBR in the presence of ADM, associated with *Spp1* overexpression in monocytes. Building on these findings, genetic manipulation of *Spp1* using transgenic *Spp1* knockout mice showed that *Spp1* expression was necessary for FBR attenuation in the presence of ADM. Finally, to translate these findings, we applied a hydrogel packaged for sustained release of recombinant SPP1 to our mouse model of FBR. Treatment as such was sufficient for rescue of the ADM capsule phenotype in the absence of ADM, further suggesting that *Spp1* overexpression, activated by the presence of ADM, is a key mechanism for attenuating FBR.

Table 1 | Summary demographics of the patients

Characteristics (paired capsule specimens)	
Age (years): mean (s.d.), range	51.5 (11.2), 35–68
Sex, *n* (%)	
Male	0 (0)
Female	10 (100)
Time to implant exchange (months): mean (s.d.), range	7 (3.9), 4–15
Expander volume: mean (s.d.), range (ml)	333 (117), 125–500
Characteristics (capsules from patients without ADM)	
Age (years): mean (s.d.), range	54 (4), 50–58
Sex, *n* (%)	
Male	0 (0)
Female	3 (100)
Time to implant exchange (months): mean (s.d.), range	10.3 (11.85), 3–24

ADM alters foreign-body capsule phenotype and decreases FBR

Capsule specimens were collected from patients undergoing expander-based breast reconstruction. During this two-stage procedure, patients first receive a tissue expander and then undergo exchange of the expander with a permanent implant following tissue expansion. Expanders were partially wrapped in ADM at the time of placement. As a result, at the time of expander–implant exchange, patients had both capsule that developed adjacent to the expander (Native capsule) and capsule adjacent to ADM (ADM capsule). These capsule specimens were retrieved from the same expander, allowing for patient-matched capsule specimens of both native and ADM capsule (Table 1). Capsule specimens were sampled at a minimum distance of 2 cm to avoid Native and ADM capsule overlap, and minimize the possibility of introducing tissue overlap as a confounding variable (Fig. 1a). Importantly, capsules were taken consistently from the posterior side of the expander pocket to minimize differences in FBR capsule due to variability in overlying tissue composition and resultant mechanical force disparities[43]. This region was also chosen to protect against any confounders from the mastectomy technique. By always collecting capsule consistently against the pectoralis major muscle, we ensured that perfusion remained consistent. Thus, these patient-matched capsules represent a rigorous comparative model for intra-individual intra-implant FBR. Clinically, the use of ADM for the purpose of decreasing FBR is rarely applied on its own without an implantable device. This model therefore reflects what is observed in patients. Collected samples were processed for histology, a multiplexed immunoassay (Luminex) and single-cell RNA sequencing (scRNA-seq).

Gross photos from specimen collection are shown in Extended Data Fig. 1a. At baseline, ADM is composed of elastin and collagen following a decellularization protocol. Hence, histological comparisons between ADM and Native capsule were normalized to ADM alone, as ADM was not dissected off the underlying tissue. On haematoxylin and eosin (H&E) histological analysis, Native capsule demonstrated denser fibrosis compared with ADM capsules (Fig. 1b). These observations were most pronounced at the superficial aspect (top) of the capsule specimen (Fig. 1b). In comparison, ADM capsule showed a looser, more porous fibrosis phenotype at the superficial aspect (top), with connective tissue integrated into the ADM layer (Fig. 1b). H&E staining of ADM alone is shown in Extended Data Fig. 1b. This finding was supported by Masson's trichrome staining of specimens, which confirmed significantly increased mean normalized collagen density in Native compared with ADM capsules (Fig. 1c, 1.4 vs 1.8, $^{*}P = 0.0122$). Normalized collagen density represents a ratio that was obtained by staining ADM alone with Masson's trichrome stain (Extended Data Fig. 1c), calculating the

mean percentage area of collagen density for ADM alone, and dividing each individual value obtained for ADM capsule and Native capsule percentage area of collagen density by this mean.

In addition, although collagen density among ADM and Native capsules was significantly different (unpaired *t*-test, $^{*}P = 0.0122$), these data did not appear sufficient to explain the previously reported clinical findings. As such, we explored additional features of fibrosis, including elastin staining and ECM ultrastructure. Elastin staining of the Native and ADM capsules was performed to interrogate the presence of additional ECM proteins. Interestingly, there was a significant increase in normalized mean elastin density found in ADM capsules relative to Native capsules (Fig. 1d, 2.0 vs 0.10, $^{****}P < 0.0001$). It has previously been observed that elastin participates in wound healing by providing mechanical elasticity, decreasing wound contracture and ultimately assisting in improved regeneration of the dermis[44]. Notably, elastin is known to confer elasticity to the ECM, thus indicating that ADM capsules are more elastic than Native capsules[45]. This increased elastin expression may provide insights into the reduced rates of pathologic capsular contracture with ADM application. Normalized elastin density via van Gieson staining, similar to normalized collagen density, represents a ratio obtained by staining ADM alone with van Gieson's stain (Extended Data Fig. 1d), calculating the mean pixel density of elastin staining for ADM alone and dividing each individual value obtained for ADM capsule and Native capsule pixel density by this mean. Quantitative analysis of ECM ultrastructure revealed that the ECMs of Native and ADM capsule exhibit notable differences[46]. Uniform manifold approximation and projection (UMAP) mapping of 294 quantified ECM ultrastructure parameters illustrated considerable divergence between ADM capsule and Native capsule ultrastructures (Fig. 1e). Thus, ECM deposition and ultrastructure analyses suggest that ADM alters multiple features of FBR fibrotic capsules. Given our previous work using ultrastructure analysis to evaluate fibrosis in human specimens[47], these data suggest that ECM analysis could be used to predict and quantify the extent of human capsular fibrosis.

To interrogate protein mediators of altered FBR with ADM use, protein isolation was performed from freshly collected human capsule specimens to assess tissue cytokine content using the Luminex multiplex immunoassay (Fig. 1f). Multiple cytokines were significantly elevated in ADM capsule (Extended Data Fig. 1e), with the greatest differences noted in stromal cell-derived factor-1 (SDF-1) a and b (mean difference 137.5, $^{**}P < 0.0096$), C-X-C motif chemokine ligand 10 (CXCL10) (mean difference 3,114, $^{**}P < 0.0066$) and interleukin-1 alpha (IL-1α) (mean difference 15.94, $^{*}P < 0.0426$)—proteins implicated in inflammation, immune cell recruitment and angiogenesis, respectively[48–50]. These changes in multiple cellular processes suggest that ADM is not only altering the fibrosis seen with capsules, but is also changing the implant environment on a broader cellular level. Finally, as fibrotic tissues tend to be stiffer, we performed functional mechanical testing of Native vs ADM capsule. This revealed that Native capsules trend towards a higher Young's elastic modulus, although it was not statistically significant (Extended Data Fig. 1f). Collectively, these data suggest that the divergence in cellular signalling may lead to the phenotypic differences in capsule formation in ADM and Native capsules.

Single-cell RNA-seq of ADM capsules reveals upregulation of *SPP1*

Given the dissimilarities observed at a histologic and chemokine level between ADM and Native capsules, we sought to explore the molecular cell signalling mechanisms underlying the phenotypic differences between Native and ADM capsules. Patient-matched human Native and ADM-adjacent capsule tissue specimens were thus subjected to scRNA-seq (Fig. 2a). scRNA-seq analysis demonstrated significant heterogeneity across all cells (Fig. 2b). Sub-analysis confirmed relative overlap between the two experimental conditions (Extended Data Fig. 2a). Further analysis centred on fibroblast and myeloid cells (macrophages and monocytes), as these cell types predominate in FBR[3].

Louvain-based (Seurat) clustering identified seven transcriptionally distinct fibroblast Seurat subclusters, with differences in contribution between Native and ADM capsules (Extended Data Fig. 2b,c). Exploring fibroblast subpopulations, two clusters with the greatest differential prevalence between ADM and Native capsules were cluster 0 (28.91% ADM vs 17.80% Native) and cluster 3 (7.03% ADM vs 19.36% Native) (Extended Data Fig. 2d). However, deeper analyses via Enrichr illustrated that both subclusters exhibited overlapping pathways and terms, including 'collagen organization', 'ECM–receptor interactions' and 'collagen-containing ECM' (Extended Data Fig. 2e)[51]. Given that few changes were observed among fibroblast subpopulations, we shifted our attention to other cell types involved in FBR: macrophages and monocytes. As it has been previously demonstrated that myeloid subpopulations play unique roles in fibrosis, we sought to interrogate the subpopulations of monocytes and macrophages within Native and ADM capsules[52–54]. For our analysis of this scRNA-seq dataset, we combined Seurat-identified macrophage and monocyte subclusters into four unique monocyte/macrophage clusters (Fig. 2c).

These monocyte/macrophage subpopulations revealed differential clustering between ADM and Native capsules (Extended Data Fig. 2f). Comparison of monocyte/macrophage Seurat clusters between ADM and Native capsules was notable for a decreased proportion of cluster 1 (5.50% ADM vs 46.60% Native) and increased proportion of cluster 2 in ADM capsules (43.10% ADM vs 6.80% Native) (Fig. 2d). Investigation of the top differentially expressed genes for each Seurat monocyte/macrophage cluster revealed Osteopontin-1 (*SPP1*) as the most differentially expressed gene in cluster 2 (fold change of 4.19, adjusted $P = 2.72 \times 10^{-65}$) (Fig. 2e,f (top) and Extended Data Fig. 2g). *SPP1* was also the highest differentially expressed gene between ADM and Native capsule monocytes/macrophages (fold change of 3.70, adjusted $P = 6.83 \times 10^{-33}$) (Fig. 2f, bottom). Further examination using pathway analysis revealed enrichment for 'HIF-1 signalling' in cluster 2 cells, a pathway that is known to be associated with tissue protection and adaptation[55]. Interestingly, this cluster also showed enrichment for 'Lipoprotein particle binding'. Lipoproteins have previously been shown to have a modulating effect on inflammatory and fibrotic disease, and the presence of this term for cluster 2 is thus suggestive of a decreased fibrotic signature in ADM capsules (Extended Data Fig. 2h, right top and bottom rows)[56,57]. In contrast, cluster 1 was enriched in Native capsule, and notable for 'complement and coagulation cascades', and

Fig. 1 | ADM alters ECM ultrastructure in human capsule specimens and leads to a reduction in fibrotic encapsulation. a, Schematic of paired capsule specimen retrieval obtained from human patients. **b**, H&E staining of ADM (left) and Native (right) capsule. Black dashed regions indicate areas from which magnified images were captured. **c**, Left: trichrome staining of ADM and Native capsule. Right: quantification of collagen density in Native and ADM capsule. **e**, Top: picrosirius red histology. Bottom: UMAP displaying quantified ECM ultrastructure parameters (ADM and Native capsule data displayed in blue and red, respectively). **d**, Left: elastin staining of ADM and Native capsule. Right: quantification of percentage of elastin+ staining in ADM and Native capsule. **f**, Left: schematic of Luminex workflow. Right: Luminex secretion assay comparing median fluorescent intensity (MFI) of SDF1A+B, CXCL10 and IL-1α secretion between Native and ADM capsules. Linked data points represent Native and ADM capsules retrieved from the same patient. **c**,**e**, Data shown as mean ± s.d.; statistical comparisons were made using unpaired two-tailed *t*-test. **f**, Data shown as absolute values; statistical comparisons were made using paired two-tailed *t*-test. $^{*}P < 0.05$, $^{**}P < 0.01$, $^{****}P < 0.0001$. Scale bars, 300 μm (**b**,**c**, top row); 60 μm (**b**,**c**, bottom row); 50 μm (**d**); 100 μm (**e**); $n = 10$ human specimens unless otherwise specified.

https://doi.org/10.1038/s41551-025-01361-4

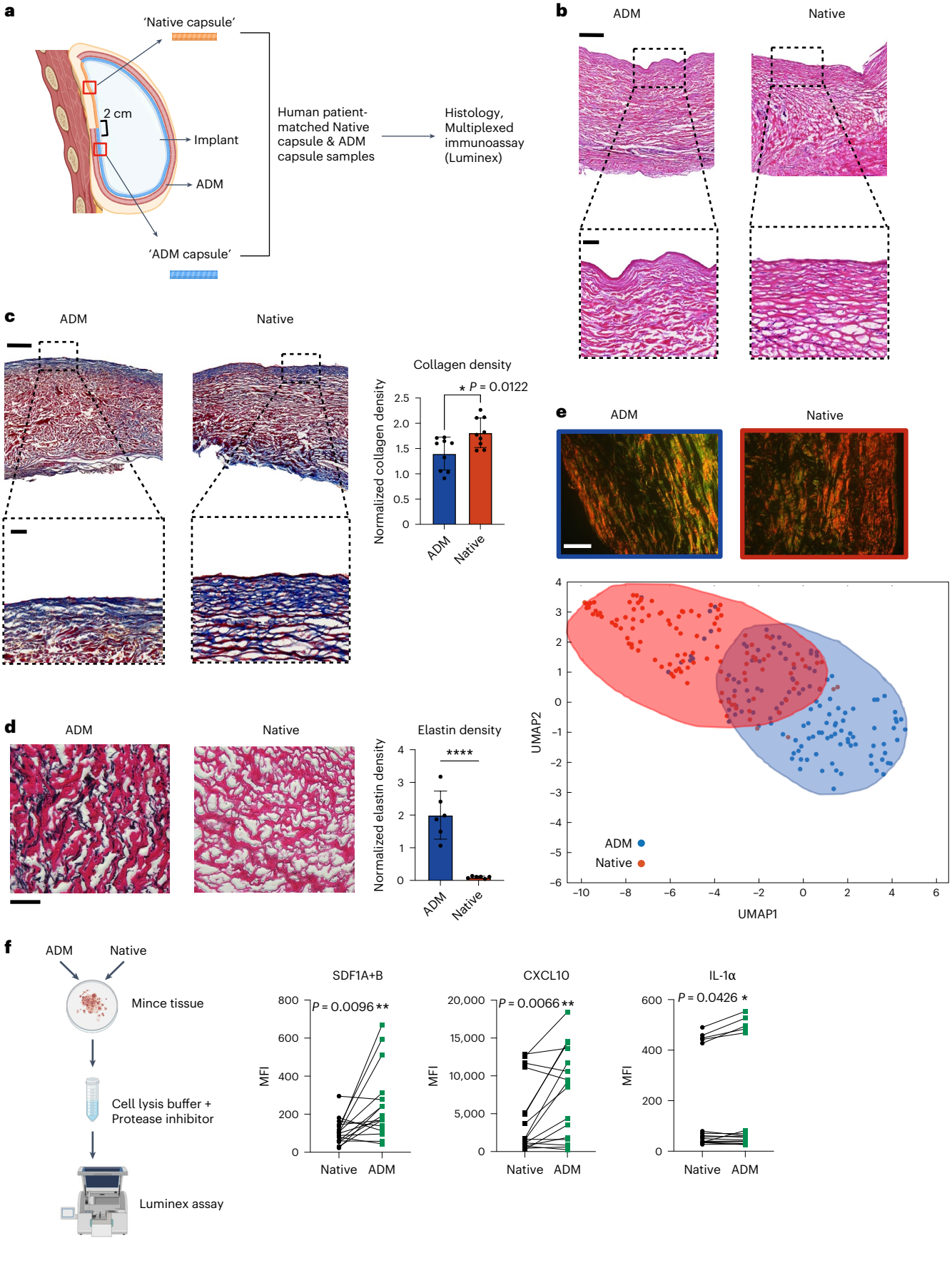

'phagosome' pathways, as well as terms including 'complement' and 'neutrophil degranulation', all suggestive of increased inflammatory signature (Extended Data Fig. 2h, left top and bottom rows). Cluster 0 and cluster 3 showed upregulation of more inflammatory terms including 'IL-1 signalling' and 'antigen presentation' (Extended Data Fig. 2i). Further subcluster analysis revealed similar changes to *SPP1* expression (Supplementary Fig. 1).

CellChat, a computational tool to investigate cell–cell communication, showed elevated interactions between diverse cell types in ADM capsules compared with Native capsules (Extended Data Fig. 3a)[58]. Cell–cell signalling pathways also differed in ADM versus Native capsules (Extended Data Fig. 3b). Interestingly, Wingless and Int-1 (WNT), neural cell adhesion molecule 1 (NCAM) and bone morphogenetic protein (BMP) signalling communication were enriched in ADM compared with non-canonical WNT (ncWNT) and receptor activator of nuclear factor kappa beta ligand (RANKL) in Native capsules (Extended Data Fig. 3b). CellChat also suggested enhanced SPP1 signalling in ADM compared with Native capsules, particularly between monocytes/macrophages, fibroblasts and endothelial cells (Fig. 2g). Increased SPP1 signalling between macrophages/monocytes, fibroblasts and endothelial cells is illustrated by the increased thickness in the brown, blue and indigo vectors in the plot.

Immunostaining further revealed significantly greater expression of SPP1 in ADM specimens compared with Native capsules in Integrin Alpha X ($CD11c^+$)-expressing cells (Fig. 2h) (***$P < 0.001$). Decreased expression of collagen type 1 (COL1) was associated with increased SPP1 expression in ADM capsules (Extended Data Fig. 3c). CD11c was selected as a marker for monocytes and macrophages as its expression was specific to those two cell populations in comparison with the pan-myeloid marker CD11b, which was also expressed in some T cells and fibroblasts (Extended Data Fig. 3d,e). SPP1 is an integrin-binding glycophosphoprotein with multiple roles in bone mineralization and tumorigenesis[59–61]. In wound healing, loss of function of SPP1 in mice has been shown to delay wound closure and cause defective macrophage infiltration. Given the parallels between fibrotic wound healing and FBR[2,3], we chose to investigate this gene further.

During the acute inflammatory phase of FBR, monocytes infiltrate the implant site and, over time, differentiate into macrophages[62,63]. As the mean time to implant exchange was 7 months, and thus beyond the acute inflammatory phase of FBR, we hypothesized that the predominant myeloid cells at this stage of FBR and chronic inflammation would be macrophages[2]. Macrophage subset analysis reinforced findings from our monocyte/macrophage analysis, demonstrating five Seurat macrophage clusters, with distinct proportional distribution of macrophage Seurat clusters between ADM and Native capsules (Extended Data Fig. 3f,g). Comparison of macrophage clusters based on experimental condition revealed relatively decreased proportions of Cluster 0 (1.2% ADM vs 47.30% Native) and Cluster 4 (6.10% ADM vs 12.40% Native) and increased proportions of Cluster 1 in ADM capsule (52.10% ADM vs 7.30% Native) (Extended Data Fig. 3h). As with monocyte/macrophage analysis findings, *SPP1* was relatively overexpressed in ADM capsule vs Native capsule (Extended Data Fig. 3i), and also emerged as a top differentially expressed gene for Cluster 1 (Extended Data Fig. 3j). Furthermore, Cluster 1 was enriched in 'phagosome', 'fibroblast growth factor (FGF) signalling' pathways and 'glycerophospholipid metabolism' GO terms (Extended Data Fig. 4a). Notably, recent literature has shown that lipid deposition profiles on the surface of biomaterials can influence FBR, with anti-fibrotic materials modifying lipid deposition and facilitating evasion of the immune response[64]. In contrast, clusters 0 and 4, more prevalent by population in Native capsules, were enriched for ECM processes including 'contraction' and 'actin cytoskeleton', as well as immune signalling, including 'interleukin 17 (IL-17) signalling' and 'nuclear factor kappa beta (NF-κβ)' (Extended Data Fig. 4a). Pathways and GO terms for clusters 2 and 3, which were found to be in similar proportions between ADM and Native capsule conditions, are illustrated in Extended Data Fig. 4b. Collectively, these data suggest that distinct SPP1+ monocyte/macrophage subpopulations may exist in ADM to reduce FBR.

Due to this work's study design, all patients received an ADM wrap; however, as there is a possibility that cells and fluids can move around an implant, which may alter signal diffusion across an implant, pathology capsule specimens from patients undergoing implant-based breast reconstruction without any ADM ('Native − ADM') were compared to Native capsule specimens (Table 1 and Extended Data Fig. 4c). Immunostaining demonstrated no significant difference in CD11c and SPP1 co-expression ($P > 0.9999$) (Extended Data Fig. 4d,e). These data provide support for the validity of this work's study design.

Spatial proteomics demonstrate differing cell–cell crosstalk

Although CellChat alongside scRNA-seq analysis and immunostaining support findings that SPP1 upregulation was observed in ADM capsule, cell–cell signalling analyses via CellChat are inference based. Thus, building upon the scRNA-seq analyses described above, we examined the spatial cell–cell profiles of ADM and Native capsules at a protein level to further validate these findings. We utilized CO-Detection by indEXing (CODEX), an assay in which a panel of 37 individual protein markers are sequentially labelled and iteratively imaged via cyclic additions and washouts of dye-labelled oligonucleotide-conjugated antibodies (Table 2 and Fig. 3a–c)[47,65,66]. This technique allows for high-throughput, multiplexed, single-cell imaging to visualize the in situ expression of cellular markers and associated cellular populations while maintaining spatial tissue architecture. Thus, CODEX permits us to build on the scRNA-seq analyses described above, to also explore changes to the spatial organization of proteins and examine the spatial cell–cell profiles of ADM and Native capsules. Across all treatment groups, 14 cell clusters were based on CODEX protein expression signatures including cluster of differentiation antigen 4 (CD4) T cells, cluster of differentiation antigen 8 (CD8) T cells, 2 endothelial clusters, 5 fibroblast clusters, 3 myeloid clusters and 2 smooth muscle cell clusters (Fig. 3b,d). Myeloid cells were defined on the basis of marker expression of CD45, CD68 and CD11c. SPP1 expression was greater in ADM compared with Native capsules, while COL1 expression was greater in Native compared with ADM capsules (Extended Data Fig. 5a). These results parallel the histologic and scRNA-seq data, wherein increased collagen was associated with increased fibrosis in Native capsule, while increased SPP1 was suggestive of the less fibrotic

Fig. 2 | Single-cell transcriptomic analyses reveal changes in monocyte/macrophage cell dynamics during foreign-body capsule formation in humans with ADM application. a, Schematic of paired capsule specimen retrieval obtained from human breast reconstruction patients followed by scRNA-seq analysis. **b**, UMAP of scRNA-seq data from all human captured cells, coloured by cell type. Black dotted region indicates cells transcriptomically classified as monocytes/macrophages (that is, in silico selection) that were used for downstream analysis. **c**, UMAP of monocytes/macrophages coloured by Seurat cluster (0–3). **d**, Relative representation of monocytes/macrophages belonging to Seurat clusters 0–3 from ADM and Native capsules. **e**, Dot plot illustrating relative expression of the top 3 differentially expressed genes in each monocyte/macrophage Seurat cluster. **f**, Violin plots showing expression of osteopontin (*SPP1*) in monocytes/macrophages by Seurat cluster (top) and experimental condition (bottom). **g**, Inferred SPP1 signalling network in cells from ADM (left) and Native (right) capsules. **h**, Top: IF staining of SPP1 (green signal) and CD11c (red signal) in Native and ADM capsules. Scale bar, 100 μm. Bottom: quantification of SPP1 and CD11c co-expression from IF staining. Data shown as mean ± s.d. ($n = 3$ regions of interest from 3 biological replicates each for human ADM and Native capsules). DAPI (4′,6-diamidino-2-phenylindole), nuclear counterstain (blue signal). ***$P < 0.001$. $n = 6$ human specimens unless otherwise specified.

https://doi.org/10.1038/s41551-025-01361-4

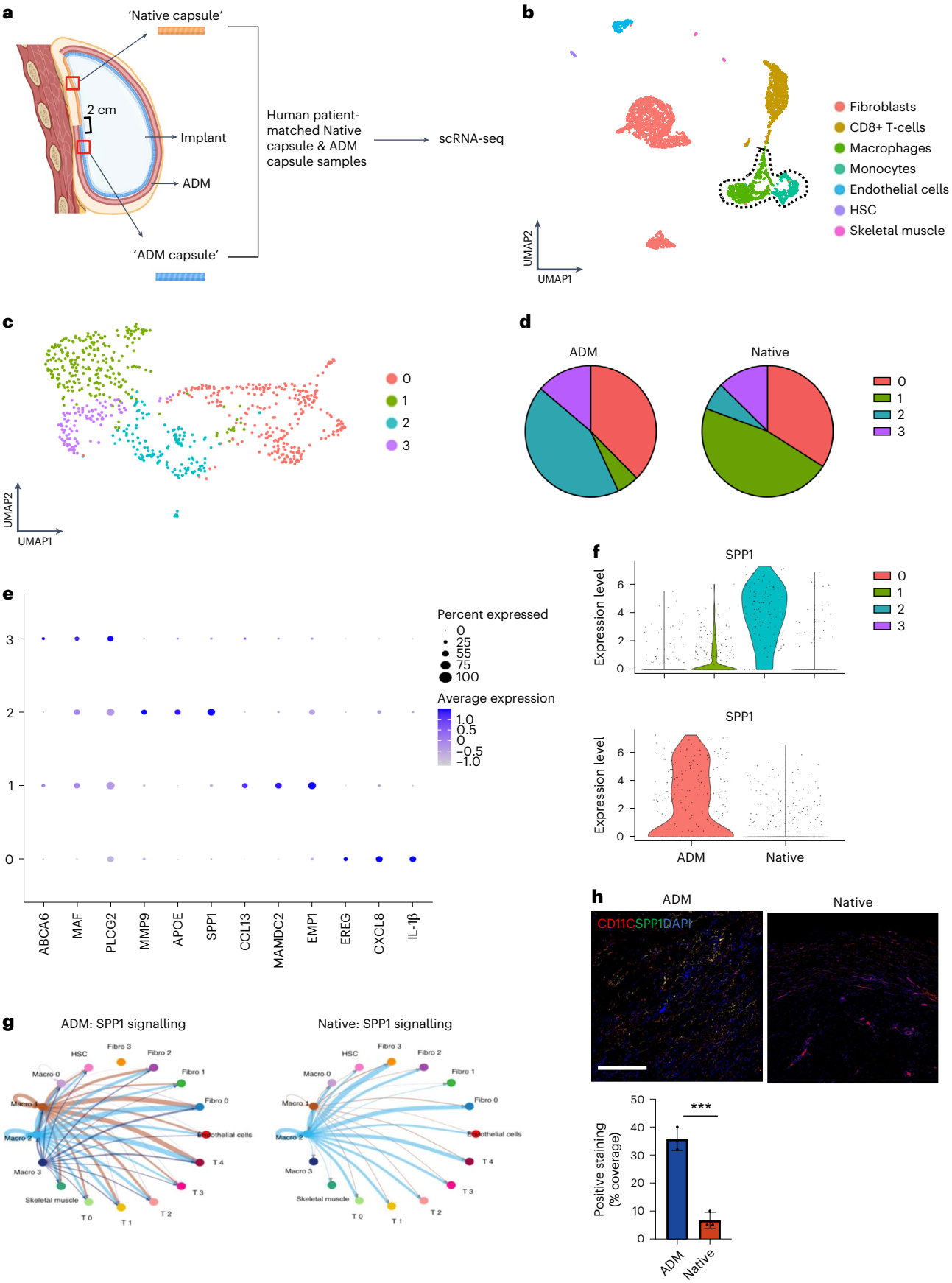

https://doi.org/10.1038/s41551-025-01361-4

Table 2 | List of protein markers and their associated barcodes for the CODEX experiment

	CODEX marker	Clone	Barcode	Company	Product no.
1	CD31	C31.3+31.7+31.10	BX001	Novus Biologicals	NBP2-47785
2	CK14	Poly19053	BX002	Akoya	SKU 4450031
3	CD4	EPR6855	BX003	Abcam	ab181724
4	YAP	EPR19812	BX010	Abcam	ab223126
5	CDH1	4A2C7	BX014	Thermo Fisher	33-4000
6	CD68	KP-1	BX015	Biolegend	916104
7	IL-6	1.2-2B11-2G10	BX016	Abcam	ab9324
8	MGP	OTI8D6	BX020	Abcam	ab273657
9	CD45	2B11+PD7/26	BX021	Novus Biologicals	NBP2-34528
10	CD11c	EP1347Y	BX024	Abcam	ab216655
11	CD8	C8/144B	BX026	Biolegend	sc-53212
12	IL-1β	Polyclonal	BX027	Abcam	ab9722
13	CD20	rIGEL/773	BX032	Novus Biologicals	NBP2-54591
14	HLA-DR	EPR3692	BX033	Abcam	ab215985
15	S100A4	S100A4	BX035	Biolegend	810101
16	FN1	Polyclonal	BX037	Abcam	ab23751
17	CD26	Polyclonal	BX040	R&D	AF1180
18	PDGFRa	16A1	BX042	Abcam	ab96569
19	COLIV	Polyclonal	BX045	Abcam	ab6586
20	α-SMA	Polyclonal	BX046	Abcam	ab5694
21	Ki67	B56	BX047	BD Biosciences	556003
22	VIM	RV202	BX049	BD Biosciences	550513
23	PANCK	AE-1+AE-3	BX019	Biolegend	914204
24	FAK	Polyclonal	BX030	Invitrogen	PA5-88093
25	MYH11	SP314	BX031	Abcam	ab240983
26	ADIPOQ	Arcp30	BX023	Novus Biologicals	NB10065810
27	PLIN1	Polyclonal	BX022	Abcam	ab3526
28	CK19	KRT19/1959R	BX025	Novus Biologicals	NBP3-08635
29	CALD1	SP226	BX028	Abcam	ab238782
30	TAGLN	Polyclonal	BX029	Abcam	ab14106
31	PDGFRB	Polyclonal	BX034	Thermo Fisher	PA5-96085
32	DES	SP138	BX041	Abcam	ab243931
33	PIEZO1	Polyclonal	BX005	Thermo Fisher	PA5-72973
34	PIEZO2	Polyclonal	BX055	Thermo Fisher	PA5-72975
35	PDPN	EPR22182	BX017	Abcam	ab2370033
36	COL1	Polyclonal	BX036	Abcam	ab34710
37	SPP1	Polyclonal	BX052	Abcam	ab283669

CD31, cluster of differentiation 31; CK14, cytokeratin 14; CDH1, E-cadherin; CD68, cluster of differentiation 68; IL-6, interleukin 6; MGP, matrix Gla protein; CD45, protein tyrosine phosphatase receptor type C; CD20, membrane spanning 4-domain A1; HLA-DR, major histocompatibility complex class II; S100A4, S100 calcium binding protein A4; FN1, fibronectin 1; CD26, dipeptidylpeptiidase IV; PDGFRa, platelet derived growth factor receptor alpha; COLIV, collagen type IV; Ki67, marker of proliferation Ki67; VIM, vimentin; PANCK, pan-cytokeratin; FAK, focal adhesion kinase; MYH11, myosin heavy chain 11; ADIPOQ, adiponectin, C1Q and collagen domain containing; PLIN1, perilipin 1; CK19, cytokeratin 19; CALD1, caldesmon 1; TAGLN, transgelin; PDGFRB, platelet derived growth factor receptor beta; DES, desmin; PIEZO1, piezo type mechanosensitive ion channel component 1; PIEZO2, piezo type mechanosensitive ion channel component 2; PDPN, podoplanin.

phenotype in ADM capsule. Given the observations made in monocytes and macrophage subclusters in our scRNA-seq dataset, we homed in on differential protein expression among myeloid subpopulations in ADM and Native capsules, which we spatially resolved at a single-cell level using CODEX. The proportions of 3 myeloid CODEX-defined clusters differed between ADM and Native capsules. ADM capsules had greater numbers of Myeloid 1 and 3 (Fig. 3e, top and bottom row), while Native capsules had greater numbers of Myeloid 2 clusters (Fig. 3e, middle row). The crosstalk between Myeloid 1 and 3 was also significantly greater in ADM versus Native capsules (Extended Data Fig. 5b). Thus, paralleling what was observed at an RNA level, myeloid cells from ADM and Native capsules differed in their protein expression as well.

Differential interaction maps were then used to visualize the strength of spatial cell–cell interactions on the basis of *K*-nearest-neighbour localization, which can be uniquely assessed using CODEX

https://doi.org/10.1038/s41551-025-01361-4

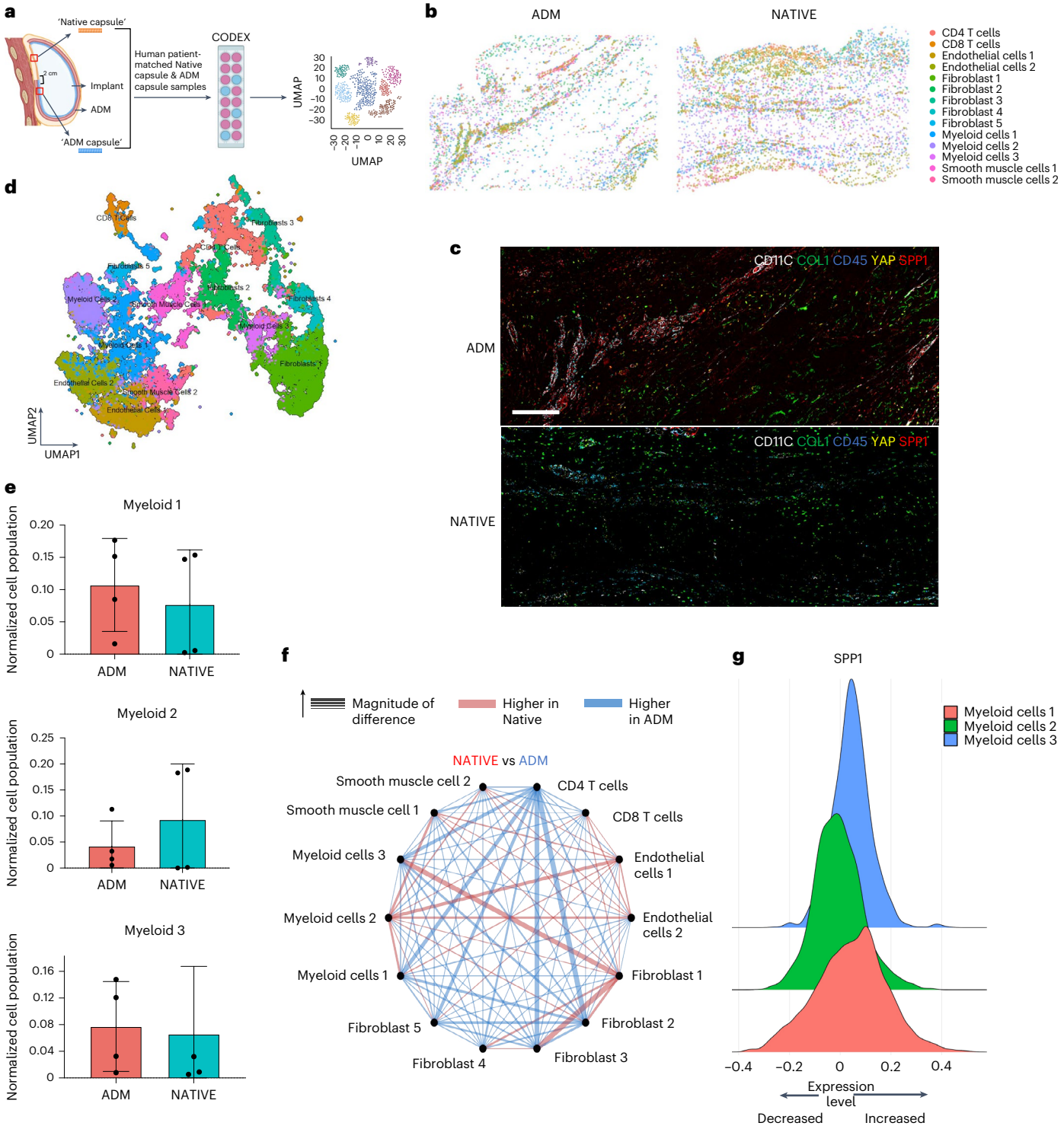

Fig. 3 | CODEX analysis of patient-matched ADM and Native human capsules. a, Schematic of the CO-Detection by indEXing (CODEX) experiment. **b**, Example of ADM and Native capsules following CODEX conjugation. **c**, Example of staining of CODEX markers in ADM (top) and Native (bottom) capsules. Scale bar, 100 mm. Images acquired for three separate regions of interest from ADM and Native capsules. **d**, UMAP of CODEX-defined clusters. **e**, Bar graph quantifying myeloid clusters in ADM and Native capsules. Data represent mean ± s.d. **f**, Differential interaction maps in Native vs ADM capsules. **g**, Ridge plot showing expression of SPP1 in myeloid clusters. $n = 3$ regions of interest each from ADM and Native capsules unless otherwise specified.

and other spatial phenotyping technologies. Cell segmentation was performed so that cell-level analyses were conducted on the basis of protein expression within the boundaries of cells. These spatial cell–cell communications were found to differ between ADM and Native capsules (Fig. 3f and Extended Data Fig. 5c). Interestingly, CODEX-defined Myeloid 2 showed strong interactions with smooth muscle cells in Native capsules (Fig. 3f and Extended Data Fig. 5d, top and bottom left). As smooth muscle cells are associated with contracture, additional crosstalk between immune cells, the acute stage of FBR and these myeloid cells, is suggestive of the increased contractile nature of fibrotic tissue from native capsule and increased fibrosis[67,68]. In contrast, CODEX-defined Myeloid 1 and 3 showed strong interactions

with CD4 cells and fibroblasts clusters (Fig. 3f and Extended Data Fig. 5d, top and bottom right).

Given the importance of *SPP1* in the scRNA-seq data, we analysed the protein expression of SPP1 in the 3 CD11c$^+$-expressing myeloid clusters. Myeloid 1 and 3 showed higher levels of SPP1 expression compared with Myeloid cluster 2 (Fig. 3g). Yes-associated protein-1 (YAP) is known to be associated with fibrosis in several organs[46,69–72]. For example, YAP signalling has been shown to play a key role in pro-fibrotic fibroblasts during wound healing[72]. YAP-mediated mechanotransduction signalling has also been implicated with inflammation and stiffness sensing in macrophages during FBR[73]. Interestingly, Myeloid cluster 2 was found to spatially express high levels of YAP. Given the established role of YAP in increased inflammation and fibrosis, elevated YAP expression in Myeloid cluster 2 may be responsible for the fibrotic phenotype in Native capsules (Extended Data Fig. 5e,f)[74]. Furthermore, smooth muscle cell clusters also demonstrated high levels of YAP1, which were found to display high crosstalk with Myeloid cluster 2 in Native capsules compared with ADM capsules (Extended Data Fig. 5e). Together, these data suggest that the spatial cell proteomic expression of ADM and Native capsules is distinct, and that spatially SPP1-expressing myeloid cells could be identified.

ADM decreases foreign-body response in a mouse model

Although we have the unique opportunity to analyse human tissue at a molecular level, to validate these findings from our patient-derived samples, we sought out an in vivo model that allowed us to modulate SPP1 in ADM and FBR. To do so, we adapted a mouse dorsal implant model[75]. C57BL/6J mice underwent dorsal implantation with sterilized 0.2 ml PDMS implants, prepared as previously detailed[76]. These implants were either placed subcutaneously without ADM on the mouse dorsum, referred to as 'mNative capsule' ($n = 6$), or covered with ADM, referred to as 'mADM capsule' ($n = 6$). Mice were divided into different experimental groups, each receiving one implant. As previously reported, a foreign-body capsule forms, encasing the implant by 21 days after surgery[75]. It has previously been shown that implant stiffness can affect the extent of fibrosis observed following implantation, where greater difference in stiffness between the implant and interface tissue causes a more extensive fibrotic response[8,9]. To establish whether there were differences in stiffness between ADM and the PDMS implants, we conducted tensile testing. No significant difference in material elastic modulus was observed between ADM and PDMS ($P = 0.2455$) (Extended Data Fig. 6a).

For our studies, we sought to characterize foreign-body capsule formation 1 month after surgery (postoperative day (POD) 28). On POD 28, capsules were collected and processed for histology (Fig. 4a). Gross images of implant placement and dissected capsule are shown in Extended Data Fig. 6b. Histologic analyses revealed analogous findings to human Native and ADM capsules by H&E and Masson's trichrome staining (Fig. 4b,c). On H&E, mNative capsule was significantly thicker than mADM capsule, with mean thickness of mNative capsules calculated to be 42.1 µm (s.d. 10.3) compared with a mean thickness of 25.9 µm (s.d. 3.5) in mADM capsules (****$P < 0.0001$, Fig. 4b). In addition, Masson's trichrome staining revealed significantly increased collagen density measured by mean area of collagen staining in mNative capsules (84.7%, s.d. 7.2), compared with mADM capsules (65.2%, s.d. 6.3, ****$P < 0.0001$, Fig. 4c). To quantify fibrotic patterns between capsule conditions, 294 ECM ultrastructure parameters were measured from picrosirius red-stained images of mNative and mADM capsules, again demonstrating divergent fibrotic phenotypes between experimental conditions (Fig. 4d), as observed in our human data. Importantly, immunostaining of capsule specimens demonstrated significantly increased alpha smooth muscle actin (α-SMA), a well-known marker of fibrosis with an established presence in FBR capsule, in mNative capsules compared with mADM capsules, mirroring patient-derived capsule phenotypes (Fig. 4e, ***$P < 0.001$)[68].

To control for potential crosstalk between PDMS and ADM, a separate cohort of mice underwent dorsal implantation with ADM alone ('ADM alone'). Histologic analyses confirmed no significant difference in capsule thickness or collagen deposition when compared to the mADM capsule condition ($P = 0.0954$ and $P = 0.0940$) (Extended Data Fig. 6c–e). Immunostaining also revealed no significant difference in α-SMA expression in ADM alone relative to mADM ($P = 0.23$) (Extended Data Fig. 6f).

Altogether, basic histology and immunostaining data collectively support that the mouse implant FBR model recapitulated the phenotypic characteristics of the patient-derived Native and ADM foreign-body capsules, with attenuated fibrosis observed with ADM.

Increased SPP1 in monocyte subclusters of mADM capsule

To explore whether application of ADM in our mouse FBR model would lead to similar transcriptional changes to those observed in the human capsules, mNative and mADM capsules were subjected to scRNA-seq at POD 28 (Fig. 5a). Similar to human samples, there was cell heterogeneity across all cells in mouse capsules (Fig. 5b), with fibroblasts and myeloid cells encompassing a large proportion of all cells. Examination of fibroblasts revealed 5 transcriptionally unique Seurat-based subclusters, with relative overlap between mNative and mADM conditions, analogous to our human dataset (Extended Data Fig. 7a,b). Two clusters with the greatest differential prevalence between mADM and mNative capsules were clusters 0 (42.98% mADM vs 34.19% mNative) and 1 (16.44% mADM vs 25.59% mNative) (Extended Data Fig. 7c); however, as with the human fibroblast clusters, Enrichr analysis highlighted that both of these clusters exhibited overlapping pathways and terms, including complement and coagulation cascades, ECM organization and collagen deposition (Extended Data Fig. 7d). Thus, as with the human dataset, we shifted our attention to macrophages and monocytes.

As we had high cell counts in both monocytes and macrophages, we chose to analyse these cell populations separately. On downstream

Fig. 4 | Murine ADM FBR model recapitulates decreased fibrosis as observed in human ADM capsule specimens. a, Silicone implants either coated with ADM (mADM) or alone (mNative) were implanted subcutaneously in the dorsi of C57BL/6j (wild-type) mice. Implant and peri-implant tissues were retrieved at POD 28 for histological analyses. **b**, Left and middle columns: H&E staining of mNative and mADM capsules. Black dashed regions indicate areas from which magnified images were captured. Yellow lines indicate capsule area. Top right: schematic representing skin layers and capsule. Bottom right: quantification of capsule thickness in mNative and mADM capsules ($n = 3$ measurements from three separate biological replicates each for mADM and mNative capsules, nine total measurements). **c**, Left and middle columns: trichrome staining of mNative and mADM capsules. Top right: schematic representing skin layers and capsule. Bottom right: quantification of collagen density in mNative and mADM capsules ($n = 3$ measurements from 3 separate biological replicates each for mADM and mNative capsules, 9 total measurements). **d**, Top: representative picrosirius red histology from mADM capsule (left, blue) and mNative capsule (right, red). Bottom: UMAP displaying quantified ECM ultrastructure parameters (mADM and mNative capsule data displayed in blue and red, respectively). **e**, Left and middle: IF staining of α-SMA (red signal) in mNative and mADM capsules. Bright red tissue is autofluorescence of panniculus carnosus. Right: quantification of α-SMA co-expression from IF staining. **b**,**c**,**e**, Data shown as mean ± s.d.; statistical comparisons were made using unpaired two-tailed *t*-test. ***$P < 0.001$, ****$P < 0.0001$. Scale bars, 100 µm (**b**,**c**, top row); 30 µm (**b**,**c**, bottom row); 50 µm (**d**); 100 µm (**e**). $n = 3$ biological replicates each for mADM and mNative capsule unless otherwise specified.

https://doi.org/10.1038/s41551-025-01361-4

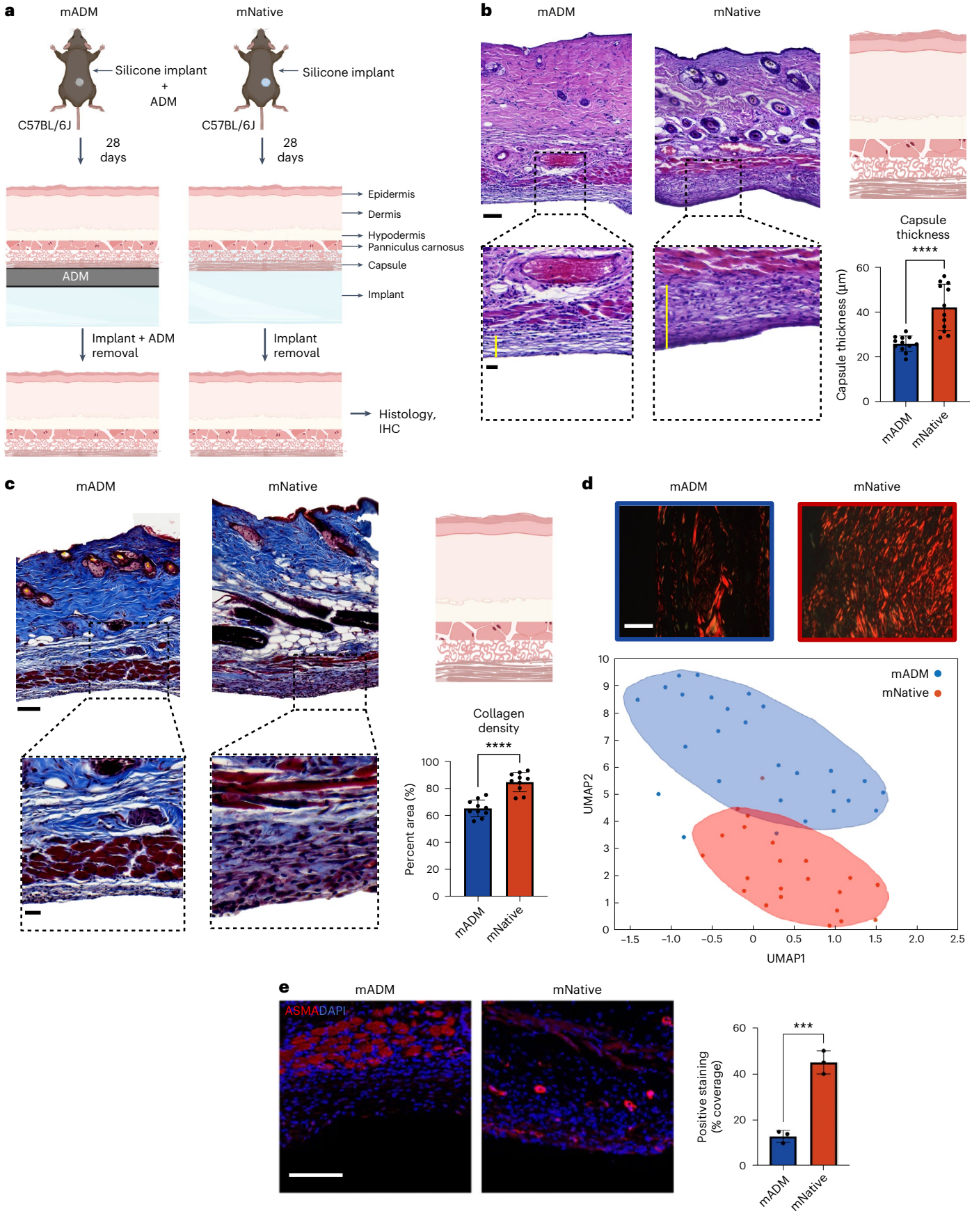

analysis, although macrophages from mADM capsules demonstrated a slight increase in SPP1 expression compared with mNative macrophages (Extended Data Fig. 7e), more striking differences in subcluster analysis were observed among monocytes, and we thus focused our analysis on the latter cell type. Once monocyte populations were isolated, we identified 7 transcriptionally unique Seurat subclusters (Fig. 5c), with partial overlap when compared by condition (Extended Data Fig. 7f).

Monocytes derived from mADM specimens showed relatively decreased proportions of clusters 2 (12.26% mADM vs 22.85% mNative) and 3 (11.00% mADM vs 17.61% mNative) and an increased proportion of cluster 4 compared with monocytes derived from mNative specimens (21.56% mADM vs 2.31% mNative) (Fig. 5d). The top differentially expressed genes from each cluster are illustrated in Fig. 5e and Extended Data Fig. 7g, with clusters 2 and 3 enriched for genes involved in inflammation, including oxidative stress-related signalling' and 'chemokine/cytokine' response. Inflammation is a key trigger for fibrosis[77] and plays a crucial role in the acute and chronic stages of FBR[3]. These clusters were also elevated in genes associated with mechanotransduction signalling pathways, such as focal adhesion kinase (Extended Data Fig. 7h). Mechanotransduction signalling is known to be a driver of fibrosis and FBR[78]. Focal adhesion kinase signalling has specifically been implicated in macrophage integrin binding to material surfaces[79,80]. Formation of focal adhesions promotes fibroblast activation and encourages the development of contractile forces[81]. Contraction and stiff ECM deposition can further activate integrins, ultimately leading to activation of TGF-β and therefore driving pro-fibrotic programmes[8]. These pathways and terms are therefore suggestive of pro-inflammatory, fibrotic function. These observations are in keeping with the inflammatory signature of human monocyte/macrophage cluster 1 (Extended Data Fig. 2h), which was enriched in Native capsule. Cluster 4 from mouse monocytes was enriched for genes involved in ECM-related GO terms, as well as with 'HIF-1 signalling' and 'vascular endothelial growth factor (VEGF) A-VEGFR2 signalling'. As stated earlier, HIF-1 signalling is known to be associated with tissue protection and adaptation[55]. Meanwhile, VEGF signalling is known to play a role in angiogenesis and tissue regeneration[82]. Notably, fibrosis often leads to dysfunctional and decreased vasculature[83,84]; thus upregulation of this transcriptional profile is suggestive of a pro-regenerative phenotype for this cluster. These data mirror those from human monocyte/macrophage cluster 2, which was enriched in ADM capsules, and are suggestive of a decreased fibrotic signature in ADM. The remaining clusters showed relatively similar proportions between mADM and mNative conditions, with respective pathways and GO terms illustrated in Extended Data Fig. 8a.

Interrogation of *Spp1* expression revealed cluster 4 to be one of 3 clusters expressing this gene (Fig. 5f, left). *Spp1* expression exhibited increased expression in mADM specimens relative to mNative specimens, reflecting findings from our human data (Fig. 5f, right). Increased SPP1 signalling was also noted between fibroblasts and myeloid cells on CellChat in ADM specimens (Fig. 5g), paralleling cell–cell interaction inference observed in our human scRNA-seq dataset. Finally, immunostaining showed significantly enhanced SPP1 and CD11c expression (Fig. 5h, $^{**}P < 0.0016$), and relatively decreased COL1 expression (Extended Data Fig. 7i) in mADM capsules compared with mNative capsules, supporting our data from patient-derived capsules. Analogous to our approach with the human dataset, CD11c was selected as a marker for monocytes as its expression was specific to this cell population in comparison with the pan-myeloid marker CD11b, which also showed more elevated expression in granulocytes, T cells and macrophages (Extended Data Fig. 7j,k).

To determine the similarity between our human and mouse datasets, we applied an anchor-based label transfer approach to project the mouse monocytes (Fig. 5) onto the human monocytes/macrophages (Fig. 2). Analysis supported a strong correlation between human monocyte/macrophage cluster 2 with high *SPP1* expression and mouse monocyte clusters 2, 3 and 4, which also had elevated *Spp1* expression and pro-fibrotic gene ontology analyses (Extended Data Fig. 8b,c). These results indicate that these mouse monocyte subclusters share a similar transcriptional programme to human monocyte/macrophage cluster 2. Further, they provide support that the mouse model recapitulates human foreign-body capsule formation at a transcriptional level. These results in conjunction with similarities between human and mouse histologic data provide further evidence of the validity of our model in providing empirical support for the earlier clinical data.

SPP1 expression is necessary for attenuation of FBR

To determine whether *Spp1* expression is necessary to attenuate FBR, we applied our murine FBR model to *Spp1* knockout (KO) mice. *Spp1* KO mice exhibit disorganized remodelling of the ECM and defective macrophage infiltration in the context of wound healing, compared with wounds in wild-type mice[85]. Histologically, the KO mice exhibit more cell debris and relatively homogeneous and smaller collagen fibrils at the site of wound healing, but this has been shown to have no effect on the tensile strength of healing incisional wounds. These observations were intriguing to us, as these attributes closely mirror features seen in FBR progression and supported our hypothesis that ADM is modulating capsule formation via *SPP1*. As such, we would expect capsule formation to occur as it would in wild-type mice, although it may appear histologically distinct. We compared FBR capsule formation under 5 conditions in *Spp1* KO mice: (1) implant only (KO mNative), (2) ADM covering the implant (KO mADM), (3) implant together with recombinant SPP1 (R&D Systems) formulated in a sustained-release hydrogel (KO +SPP1), (4) ADM covering implant with hydrogel-delivered recombinant SPP1 (KO mADM +SPP1) and (5) ADM covering implant with a non-drug-loaded empty hydrogel (KO mADM −SPP1) (Fig. 6a and Extended Data Fig. 10a)[86]. Given the observations made on human and mouse scRNA-seq datasets, we aimed to establish how capsule composition changed with ADM in the absence of *Spp1*, hypothesizing that the capsule would revert to an mNative state. To further confirm that the absence of *Spp1* caused the change to capsule composition in this experimental group, the implant together with recombinant SPP1 as well as the implant coated with ADM together with recombinant SPP1 were evaluated in *Spp1* KO mice. Finally, the implant coated with ADM together with the non-drug-loaded empty hydrogel acted as a negative control to confirm that the gel itself did not alter FBR.

Fig. 5 | Single-cell transcriptomic analyses comparing murine Native and ADM capsules mimic myeloid cell dynamics in human FBR. a, Silicone implants either coated with ADM (mADM) or alone (mNative) were implanted subcutaneously in the dorsi of C57BL/6J (wild-type) mice. Implant and peri-implant tissues were retrieved at POD 28 for scRNA-seq. **b**, UMAP of scRNA-seq data from all mouse capsule cells, coloured by cell type. Black dotted region indicates cells transcriptomically classified as monocytes (that is, in silico selection) that were used for downstream analysis. **c**, UMAP of monocytes coloured by Seurat subcluster (0–6). **d**, Relative representation of monocytes belonging to Seurat subclusters 0–6 from mNative and mADM capsules. **e**, Dot plot of relative expression of the top 2 differentially expressed genes in each monocyte Seurat subcluster. **f**, Violin plots showing expression of osteopontin (*Spp1*) in monocytes by Seurat subcluster (left) and experimental condition (right). **g**, Inferred SPP1 signalling network in cells from mADM (top) and mNative (bottom) capsules. **h**, Left and middle: IF staining of SPP1 (green signal) and CD11c (red signal) in mADM and mNative capsules. Bright green tissue is autofluorescence of panniculus carnosus. Right: quantification of SPP1 and CD11c co-expression from IF staining. Data shown as mean ± s.d.; statistical comparisons were made using unpaired two-tailed *t*-test. $^{**}P < 0.01$. Scale bar, 100 µm. $n = 3$ biological replicates each for mADM and mNative capsules.

https://doi.org/10.1038/s41551-025-01361-4

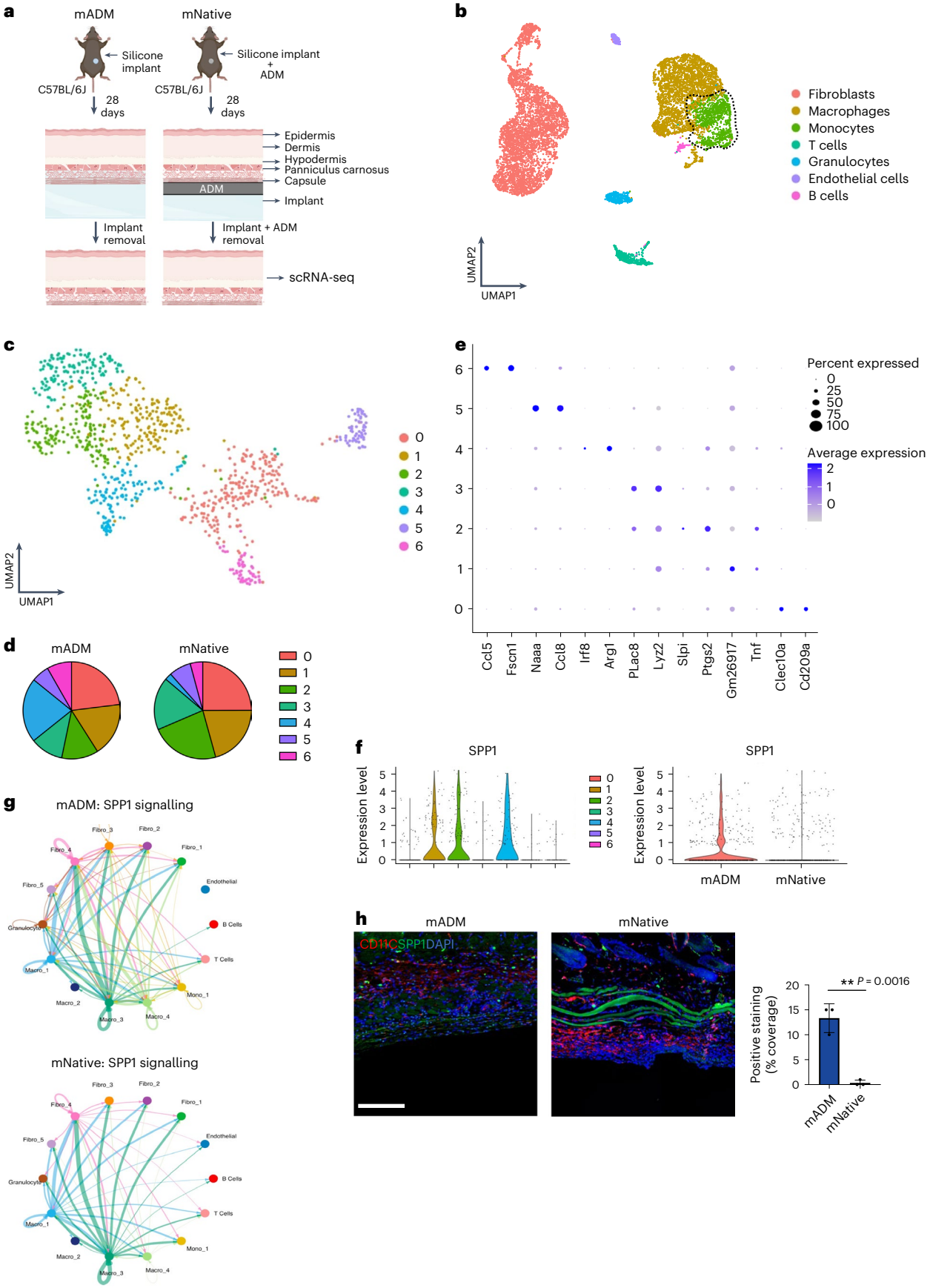

This polymer-nanoparticle (PNP) hydrogel is easily injectable and rapidly self-heals, limiting cargo burst release, and has excellent biocompatibility in several species (rodents, sheep and rabbits)[87–90]. The PNP hydrogel has previously been shown to facilitate slow release of a variety of cargos, including cells, small molecules and proteins such as the receptor-binding domain of the SARS-CoV-2 spike protein, which is of comparable molecular size to SPP1 (refs. 89–94). In vitro studies of SPP1-formulated PNP hydrogel confirmed sustained release of SPP1 over the course of a month at physiologic temperature, with a half-life of 16 days (Extended Data Fig. 9a). As softer materials have been shown to elicit less-severe FBR[8], to avoid introducing a confounding variable with application of the gel, we specifically injected it as a sustained-released drug depot adjacent to the implant.

On histological analysis, no significant differences in capsule thickness or collagen density between KO mNative specimens and KO mADM specimens were observed (Fig. 6b,c). KO +SPP1 capsules, however, measured a mean of 20.4 µm (s.d. 4.3) and were significantly thinner compared with KO mNative capsules (mean 47.5 µm, s.d. 7.9; $^{****}P < 0.0001$) or KO mADM capsules (mean 48.9 µm, s.d. 12.9; $^{****}P < 0.0001$) (Fig. 6b). Similarly, collagen density, measured as percent area, was significantly lower in KO +SPP1 capsules (mean 54.2%, s.d. 28.5) compared with KO mNative capsules (mean 98.0%, s.d. 1.4; $^{***}P < 0.001$) or KO mADM capsules (mean 96.8%, s.d. 3.3; $^{***}P < 0.001$) (Fig. 6c). Ultrastructural analysis of 294 unique ECM features using picrosirius-red-stained capsules revealed overlap of KO mNative and KO mADM capsules. Meanwhile, KO +SPP1 capsules were distinct in UMAP space relative to the remaining experimental groups (Extended Data Fig. 9b). Immunostaining showed increased SPP1 expression in CD11c-co-expressing cells and decreased fibrotic marker expression (α-SMA and COL1) in KO +SPP1 capsules relative to KO mNative and KO mADM capsules (Fig. 6d, $^{***}P < 0.001$ compared to KO mNative and $^{*}P = 0.0101$ compared to KO mADM; Extended Data Fig. 9c, $^{***}P < 0.001$ for both).

Comparing capsule thickness, KO mADM +SPP1 (mean 19.3 µm, s.d. 3.567) capsules were significantly thinner than KO mADM −SPP1 capsules (mean 47.84 µm, s.d. 11.95; $^{****}P < 0.0001$) (Extended Data Fig. 10b). Similarly, collagen density was significantly lower in KO mADM +SPP1 capsules (mean 44.85%, s.d. 19.09) relative to KO mADM −SPP1 capsules (mean 93.92%, s.d. 3.971; $^{****}P < 0.0001$) (Extended Data Fig. 10c). KO mADM +SPP1 capsule thickness and collagen density paralleled those of KO +SPP1 capsules (Fig. 6b,c), while KO +mADM −SPP1 capsule thickness and collagen density paralleled those of KO −SPP1 and KO mADM capsules (Fig. 6b,c). Upon picrosirius red staining, KO mADM +SPP1 displayed similar architectural properties to KO +SPP1 capsule specimens (Extended Data Figs. 9b and 10d). Immunostaining showed decreased fibrotic marker expression (α-SMA and COL1) in KO mADM +SPP1 capsules (Extended Data Fig. 10e,f, $^{**}P = 0.0048$ and $^{**}P = 0.0011$, respectively), as well as increased SPP1 expression in CD11c-co-expressing cells (Extended Data Fig. 10f).

Thus, these five experimental groups support that SPP1 expression may be necessary for inducing the attenuated fibrotic capsule phenotype normally seen in ADM and mADM capsules in wild-type mice.

Sustained release of SPP1 sufficient to decrease FBR in mice

Having established that SPP1 was necessary to decrease fibrotic capsule formation in our murine FBR model, we next investigated whether sustained release of recombinant SPP1 in a wild-type mouse would be sufficient to recapitulate the observed phenotypic change upon ADM application, as genetic knockouts are not clinically translatable. To this end, we treated wild-type C57BL/6J mice with: (1) implant together with empty PNP hydrogel without recombinant SPP1 (mNative −SPP1); (2) ADM-covered implant (mADM) as our positive control; or (3) implant together with recombinant SPP1-loaded PNP hydrogel (mNative +SPP1) (Fig. 6e). As before, gel was injected as a sustained-released drug depot adjacent to the implant to avoid changing the stiffness of the implant at the tissue interface.

Histology revealed significantly decreased capsule thickness and collagen density in mNative +SPP1 capsules relative to mNative −SPP1 capsules. No significant difference in capsule thickness was observed between mNative and mNative −SPP1 groups, indicating that the depot gel alone did not impact FBR ($P = 0.0534$). Although capsule thickness was greater in mNative +SPP1 capsules compared with mADM capsules, collagen density measurements were comparable between these two groups (Fig. 6f,g). Mean mNative +SPP1 capsule thickness was 30.9 µm (s.d. 4.9), compared with 50.0 µm (s.d. 6.7; $^{****}P < 0.0001$) in mNative −SPP1 capsules and 26.2 µm (s.d. 2.7; $^{**}P = 0.0022$) in mADM capsules (Fig. 6f). Mean percent area of collagen density was significantly lower in mADM (29.5%, s.d. 15.3) and mNative +SPP1 (30.3%, s.d. 9.9) capsules compared with mNative −SPP1 capsules (75.7%, s.d. 16.8; $^{****}P < 0.0001$ and $^{***}P < 0.001$, respectively), and there was no difference between mADM and mNative +SPP1 with respect to collagen density ($P = 0.99$, Fig. 6g). ECM ultrastructural analysis of 294 unique parameters on picrosirius-red-stained capsule specimens revealed overlap of capsule ultrastructure of mADM and mNative +SPP1 capsules, and divergence from mNative −SPP1 capsule (Extended Data Fig. 9d). Immunostaining

Fig. 6 | Osteopontin (SPP1) is both necessary and sufficient to decrease fibrotic encapsulation due to foreign-body response. a, Schematic of experimental flow of the murine FBR model used. Silicone implants either alone (KO mNative), coated with ADM (KO mADM) or combined with an ipsilateral injection of recombinant SPP1-loaded PNP hydrogel (KO +SPP1) were implanted subcutaneously in the dorsi of *Spp1* knockout (SPP1 KO) mice. Implant and peri-implant tissues retrieved at POD 28 for histologic analyses. **b**, Left: H&E staining of KO mNative, KO mADM and KO +SPP1 capsules. Black dashed regions indicate areas from which magnified images were captured. Yellow lines indicate capsule area. Top right: schematic representing skin layers and capsule. Bottom right: quantification of capsule thickness in KO mNative, KO mADM and KO +SPP1 capsule. **c**, Left: trichrome staining of KO mNative, KO mADM and KO +SPP1 capsules. Black dashed regions indicate areas from which magnified images were captured. Top right: schematic representing skin layers and capsule. Bottom right: quantification of collagen density in KO mNative, KO mADM and KO +SPP1 capsule. **d**, Top and bottom left: IF staining of α-SMA (red signal) in KO mNative, KO mADM and KO +SPP1 capsule. Bottom right: quantification of α-SMA expression from IF staining. **e**, Schematic of experimental flow of the murine FBR model used. Silicone implants either combined with an ipsilateral injection of empty PNP hydrogel (mNative −SPP1), coated with mADM or combined with an ipsilateral injection of recombinant SPP1-loaded PNP hydrogel (mNative +SPP1) were implanted subcutaneously in the dorsi of C57BL/6J (wild-type) mice. Implant and peri-implant tissues retrieved at POD 28 for histologic analyses. **f**, Left: H&E staining of mNative −SPP1, mADM and mNative +SPP1 capsules. Black dashed regions indicate areas from which magnified images were captured. Yellow lines indicate capsule area. Top right: schematic representing skin layers and capsule. Bottom right: quantification of capsule thickness in mNative −SPP1, mADM and mNative +SPP1 capsules. **g**, Left: trichrome staining of mNative-SPP1, mADM and mNative +SPP1 capsules. Black dashed regions indicate areas from which magnified images were captured. Top right: schematic representing skin layers and capsule. Bottom right: quantification of collagen in mNative −SPP1, mADM and mNative +SPP1 capsules. **h**, Top and bottom left: IF staining of α-SMA (red signal) in mNative −SPP1, mADM and mNative +SPP1. Bottom right: quantification of α-SMA expression from IF staining. Bright red tissue is autofluorescence of panniculus carnosus. (**b**–**d**,**f**–**h**) Data shown as mean ± s.d. $^{*}P < 0.05$, $^{**}P < 0.01$, $^{***}P < 0.001$, $^{****}P < 0.0001$; NS, not significant. Scale bars, 50 µm (**b**,**c**,**f**,**g**, bottom rows); 100 µm (**b**,**c**,**f**,**g**, top rows); 50 µm (**d**,**h**). $n = 4$ measurements from 3 separate biological replicates each for mADM and mNative capsules, 12 total measurements (**b**,**c**,**f**); $n = 3$ measurements from 3 separate biological replicates each for mADM and mNative capsules, 9 total measurements (**g**); $n = 3$ biological replicates for each condition (**d**,**h**). Statistical comparisons were made using repeated measure one-way ANOVA with Turkey's correction for multiple comparisons (**b**,**c**,**f**,**g**) or ordinary one-way Anova with Bonferroni correction for multiple comparisons (**d**,**h**).

https://doi.org/10.1038/s41551-025-01361-4

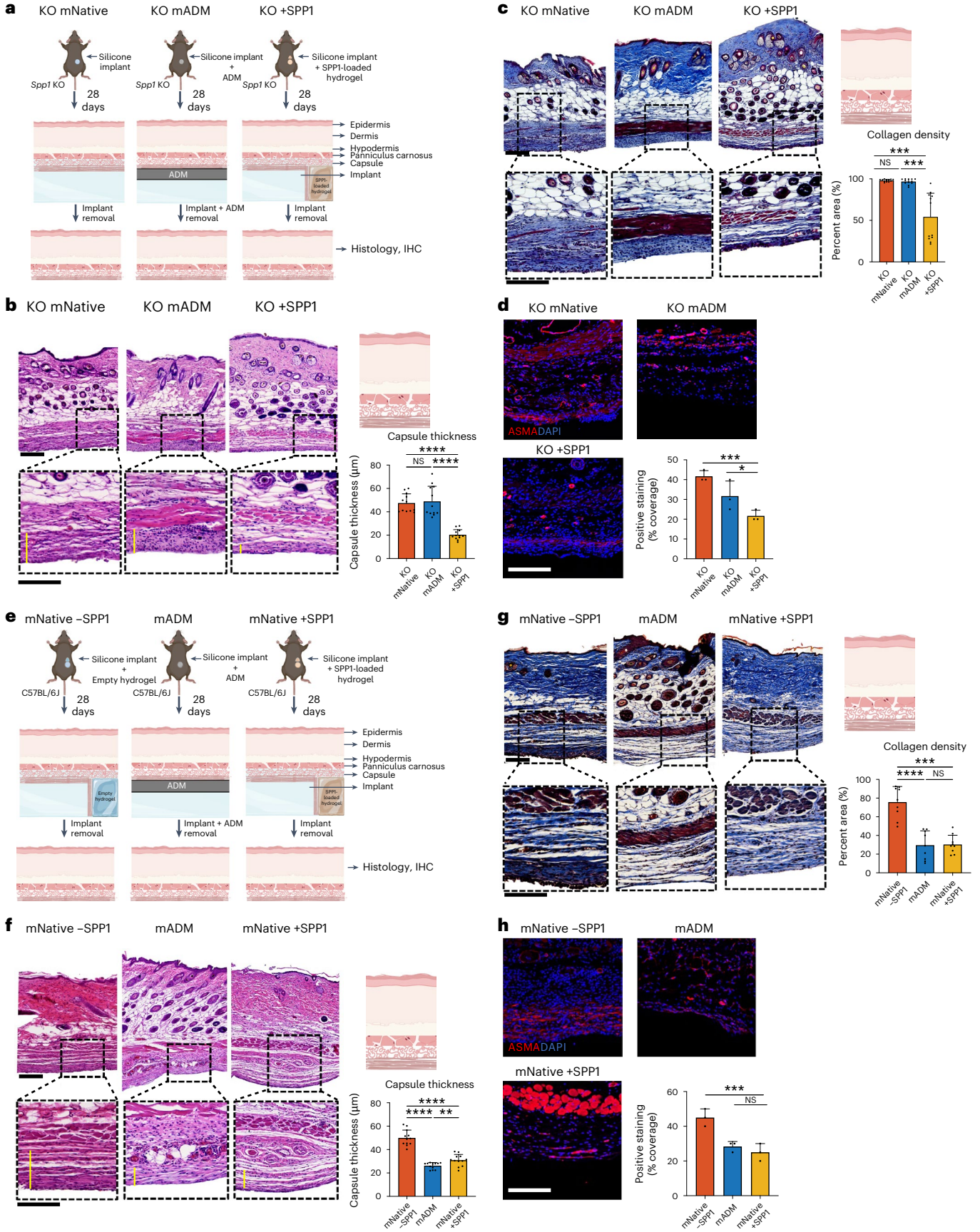

confirmed decreased α-SMA and COL1 expression in mNative +SPP1 and mADM relative to mNative −SPP1 capsules (Fig. 6h, $^{**}P = 0.0043$ and $^{*}P = 0.0107$; and Extended Data Fig. 9e, $^{*}P = 0.0242$ for both conditions). Immunostaining also showed increased SPP1 expression in CD11c-expressing cells in mNative +SPP1 and mADM relative to mNative −SPP1 capsules (Extended Data Fig. 9e). Collectively, these data support that SPP1 release could substitute for ADM and is sufficient to restore the attenuated fibrotic capsule phenotype in our murine FBR model.

To evaluate whether SPP1 recombinant protein caused any toxicity, SPP1 resuspended in PBS was injected subcutaneously every other day for 28 days in an otherwise healthy, wild-type mouse. As observed on H&E staining, no visible toxicity was observed, with all expected skin architecture and associated appendages present (Extended Data Fig. 9f). To ensure that the hydrogel on its own did not influence capsule formation, an additional group of wild-type C57BL/6 mice received implants and injections of SPP1 resuspended in PBS every other day for 28 days (mNative +SPP1 PBS) (Extended Data Fig. 9g). Relative to the implant alone control, capsule thickness and collagen density in mNative +SPP1 PBS were significantly reduced (mean 33.68 µm, s.d. 5.496; $^{*}P = 0.0377$ and mean 47.78%, s.d. 12.52; $^{****}P < 0.0001$, respectively) (Extended Data Fig. 9h,i). Immunostaining showed significantly reduced α-SMA expression in mNative +SPP1 PBS relative to the control group as well ($^{*}P = 0.0064$) (Extended Data Fig. 9j). These data suggest reduced fibrosis as a result of SPP1, in keeping with the results observed with the sustained-released SPP1-loaded gel.

SPP1 is well known to interact via two separate pathways. First, it has been shown that SPP1 can bind to integrin αvβ3 and activate integrin-mediated signalling[33,39]. Second, SPP1 can activate downstream gene expression via CD44 (refs. 42,95). Investigation of expression of *Integrin Subunit Alpha V* (*ITGV5*) and *Integrin Subunit Beta 3* (*ITB3*) genes encoding for subunits of integrin αvβ3 suggested expression of only one of the two subunits and only in Seurat cluster 2 of human monocytes/macrophages (Extended Data Fig. 10g). In contrast, CD44 showed expression across all subclusters of human monocytes/macrophages (Extended Data Fig. 10h) and was confirmed at a protein level via immunostaining (Extended Data Fig. 10i). Interestingly, *MMP9*, a known direct downstream target of SPP1-CD44 signalling, was expressed at significantly higher levels in ADM capsule monocytes/macrophages relative to Native capsule monocytes/macrophages (log fold change 1.57, adjusted $P = 6 \times 10^{-10}$) (Extended Data Fig. 10j). Staining via IF confirmed increased protein expression of MMP9 ($^{*}P < 0.0287$) (Extended Data Fig. 10k). Thus, these data may suggest a potential mechanism by which *SPP1* acts, by binding CD44 and activating its downstream target, *MMP9*.

Discussion

Since the biomaterial's initial use in the early 2000s, ADM's applications have grown in breadth and frequency, with clinical studies correlating its application with decreased capsular contracture and improved native tissue integration; however, the molecular mechanisms responsible for this biomaterial's beneficial properties remain elusive. Applying ADM as a case study to understand the mechanisms underlying fibrotic encapsulation, this work evaluated patient-matched specimens from human patients alongside supportive investigations in murine FBR models. Using a molecular approach, we have shown via histologic, transcriptomic and proteomic studies that ADM use leads to an upregulation of SPP1 signalling in monocytes and macrophages, ultimately decreasing fibrotic encapsulation as a result of FBR. These data were supported with a loss-of-function experiment wherein ADM-coated implants placed in *Spp1* constitutive knockout mice mimicked Native capsule, supporting that *Spp1* expression is necessary for this ADM-associated phenotype. Finally, when a slow-release SPP1-loaded hydrogel was added to our wild-type mouse FBR model, it resulted in reduced fibrotic capsule formation. This reduction was similar to the effects observed with ADM capsules, providing evidence that overexpression of SPP1 alone is enough to mimic the effects of ADM on FBR.

SPP1 is an integrin-binding glycophosphoprotein that has been shown to play significant roles in cancer, bone homeostasis and metabolism[33,39,96]. In addition, SPP1 has been shown to also bind and mediate signals via CD44 in hair follicle stem cells[42]. Associated with tumour progression, invasion and metastasis, elevated expression levels of SPP1 have been connected with poor prognosis; yet, how it relates to gene mutation and immune cell infiltration is not well understood[39]. Some reports have shown *SPP1* to be associated with fibrotic outcomes, including FBR. For example, in a study exploring FBR as a result of different material classes demonstrated that *SPP1* was one of the highest-expressed genes[97]. Mirroring these results, a group exploring FBR-associated transcriptome demonstrated a collection of hub genes associated with FBR, including *SPP1* (ref. 37). However, as these groups did not explore gene expression at a single-cell level, we are left to speculate that perhaps elevation of SPP1 expression within specific cell types may lead to the decreased fibrosis associated with ADM. In support of this hypothesis, it has been previously shown that SPP1 knockout mice demonstrated increased foreign-body giant cells relative to implanted wild-type controls, while addition of soluble SPP1 led to reduced macrophage fusion[38]. As foreign-body giant cells are a key indicator of the inflammation of FBR that eventually leads to fibrosis, these results strongly suggest a parallel to the decreased response we observe with application of ADM.

In specific conditions, upregulation of *SPP1* has previously been demonstrated to decrease fibrosis in certain organ systems. Notably, one recent study established that macrophage-derived *SPP1* upregulation led to activation of STAT3 signalling and had an overall protective effect on non-alcoholic steatohepatitis[40]. Further, multiple studies indicate that *SPP1* expression is important for muscle regeneration following injury[41,98,99]. Thus, SPP1 signalling may play both fibrotic and anti-fibrotic roles depending on the organ pathology, and further investigations will be needed to distinguish between pro-regenerative and pro-fibrotic mechanisms.

A key finding from our investigations suggests that upregulation of *SPP1* leads to a reduction in fibrotic encapsulation following FBR. Nevertheless, limitations to this study remain. In particular, for both the human capsule samples along with those retrieved from our murine FBR model, we made use of silicone-based implants. Given the breadth of biomaterials used in surgery (for example, ceramic, titanium, polyurethane), understanding whether SPP1 signalling can reduce FBR in non-silicone biomaterials will be of clinical interest. For example, in orthopaedics, many of the materials used for total joint replacements include ceramic, metal and polyethylene-based biomaterials. These replacements invoke a foreign-body reaction that has been associated with periprosthetic osteolysis, loss of bony support, and loosening and subsequent failure of the implant[4]. Similarly, as multiple observations have been made that implant material and stiffness affect the extent of FBR[8], further investigations into how SPP1 may affect biomaterial mechanical properties is warranted. These mechanical considerations will be important for potential clinical translation. Investigating specifically how differences in biomaterial stiffness might impact SPP1 expression is also warranted. Multiple groups have previously demonstrated that increased extracellular matrix stiffness leads to or is associated with upregulation of *SPP1* expression in urinary and hepatic cancers[100–102]. As mentioned, given that SPP1 signalling may play both fibrotic and anti-fibrotic roles, how these observations may impact foreign-body response outcomes when applying SPP1 protein to materials of different stiffness is worth further investigation.

Given that the majority of our work was conducted in a small animal model, the potential application of recombinant SPP1 administration in reducing FBR would require further translational investigations for safety and dosing evaluation. As ADM is typically

decellularized human cadaveric dermis, it will be important to investigate the potential effects that species-specific ECM matrix proteins have or whether post-translational modifications in ADM remain for further in vivo animal studies exploring the underlying mechanism of ADM and FBR attenuation[103]. For example, species-specific post-translational glycosylation modifications have been shown to alter immune-mediated responses[104]. Although histologic and transcriptomic data from mouse studies recapitulated what was observed in the human samples, these modifications could lead to a change in the response observed. Conducting a glycosylation analysis of ADM to identify human-specific glycosylation sites present in ADM via mass spectrometry may indicate off-target immunologic effects when utilized in experimental procedures in mice[105]. There is also a possibility that cells and fluids can move around an implant, and this may alter signal diffusion across an implant. Due to this work's study design, we did not have the opportunity to collect non-patient-matched capsule specimens, as all patients undergoing expander-based breast reconstruction received an ADM wrap. Although significant differences at histologic, transcriptomic and proteomic levels were observed between conditions, further investigations include exploring the possibility of native capsule signals reaching and affecting ADM-treated regions and vice versa. It is possible that additional differences at transcriptomic and proteomic levels could be observed had capsules been retrieved from different pockets entirely, as potential mingling between Native and ADM capsules could dampen observed changes. Alternatively, there is a chance that the interaction between ADM and PDMS materials specifically may have caused some of the histologic and molecular differences seen among experimental groups. From a clinical standpoint, certain pathologic diagnoses such as BIA-ALCL involves lavage and washout of the breast implant pocket[106]. For further applications in the context of neoplasms, the inclusion of two material systems may make understanding the underlying pathology more difficult. In addition, tissue composition and mechanical force disparities may affect FBR capsule formation[43]. Although chosen as this was the most consistent collection site among patients, posterior wall capsule may be different from other regions and may not fully reflect FBR processes elsewhere. Further investigation into the application of ADM and SPP1 function in other tissue types and regions will help broaden the scope of this work beyond applications in reconstructive surgery.

From a technical standpoint, although the application of inference-based analyses such as CellChat offers valuable insights into potential cell–cell interactions, some caution needs to be taken when interpreting these data without further experimental evidence. Similarly, within our human dataset, differences in captured cell counts were observed between Native and ADM groups. This may have resulted in size-associated trends that cannot be removed via standard scaling normalization. This difference in cell count may also make visualization of these data and their overlap in UMAP space more challenging. To overcome this, we incorporated downsampling computational tools (Supplementary Fig. 1) to confirm that cell counts were not a confounding factor for downstream analysis. Our downsampling analysis further suggested that *SPP1* expression remained upregulated in ADM monocytes and macrophages relative to those from Native. On the other hand, given the computationally stochastic nature of downsampling using our approach, choosing to downsample before data analysis may lead to a loss of cells of interest in a given dataset, and thus limit downstream data analysis.

Moreover, CODEX is limited to a panel of proteins (~100 at time of writing), which requires the user to be selective with the makers chosen. For example, the markers utilized in the CODEX panel used to define myeloid cell types were CD45, CD68 and CD11c. These markers have overlap between macrophages, monocytes and dendritic cells, which made it challenging to further define myeloid subpopulations. Additional explorations on the specific types of myeloid cells involved in decreasing FBR with application of ADM at a protein-specific level will further our mechanistic understanding of this process. Moreover, we placed the SPP1 within a hydrogel adjacent to the implant. Developing an implant from which the SPP1 is released directly from its surface would enhance the clinical translation of this protein. As it is well known that protein adsorption is specific to both the biomaterials and protein applied[107], further investigation on the effect of SPP1 adherent to other biomaterials will be needed to confirm a similar biological response and optimize a translational approach.

In summary, we used clinical and mouse models to establish molecular pathways that may provide therapeutic targets to overcome the FBR. Through a histologic and transcriptomic approach, we provide evidence for a potential mechanism by which ADM may alter the implant microenvironment and change the resulting fibrotic capsule. Interestingly, as *Spp1* expression differed most strikingly among monocytes as opposed to all myeloid-lineage cells within the mouse scRNA-seq data, we are led to hypothesize that ADM may function via modulation of monocytes, specifically. Future work should further explore the mechanistic drivers of SPP1 upregulation and investigate the possibility that this modulation occurs within certain myeloid-lineage targets. Finally, with deeper understanding of the underlying biology of ADM-modulated FBR, there may be exciting opportunities to modulate these drivers in broader contexts.

Methods

Mice

Transgenic mouse strains (acquired from Jackson Laboratories): B6 (C57BL/6J, 000664), Spp1KO (B6.129S6(Cg)-Spp1tm1Blh/J, 004936). Mice were housed at the Stanford University Comparative Medicine Pavilion following Stanford APLAC guidelines (APLAC 34177) under the supervision of the Veterinary Service Center (VSC). Mice were provided rodent chow and water ad libitum, and were kept in temperature, humidity and light-regulated (12 h dark/light cycling) housing.

Male and female mice in equal numbers between 8 and 12 weeks of age were used. A minimum of 3 mice and upwards of 6 per condition per experiment were used.

Patient sample collection

All patients undergoing tissue expander-based breast reconstruction implant exchange by a single plastic surgeon (Dr Arash Momeni) were informed of the Stanford University institutional review board-approved study ($n = 10$). For those patients who wished to provide consent for involvement in the study, patient demographics and medical history were recorded in a secure encrypted database. The senior surgeon performed an incomplete ADM wrap of tissue expanders at the time of first-stage tissue expander pre-pectoral reconstruction. Thus, capsule specimen could be obtained from (1) the periprosthetic capsule that develops adjacent to the expander (hereafter referred to as 'native capsule') but distinct from the ADM capsule and (2) from the capsule that develops adjacent to the ADM (hereafter referred to as 'ADM capsule'). At the time of tissue expander–implant exchange, a 3 × 1-cm area of native and ADM capsules were obtained and divided into three smaller portions for (1) histological analysis, (2) fluorescence-activated cell sorting (FACS) and transcriptomic analysis and (3) proteomic analysis. Intra-operatively, capsule specimens were obtained from the native capsule and the ADM capsule. The ADM capsule was removed with the ADM attached, as it was well integrated into the surrounding tissues. If the ADM was not incorporated, the patient's samples were excluded from analysis. An additional three capsule specimens were collected for patients who underwent tissue expander–implant exchange without ADM wrap. Patient demographic information is presented in the lower half of Table 1.

Participants did not receive compensation for their participation in the study.

Acellular dermal matrix preparation

ADM (Alloderm RTM, LifeCell) was donated from leftover operating room materials. The ADM was stored in PBS at 4 °C for up to 4 weeks in a sterile environment. Before implantation in the mouse, the ADM underwent 3 phosphate buffered saline (PBS) washes to remove any remaining associated preservative. Following washing, the ADM was cut into 1 cm × 1 cm squares with sterile surgical scissors.

Implant fabrication

Implants were fabricated using a modified method as previously reported[1]. Briefly, hemispherical 0.2 ml implants were created by casting Sylgard 184 (Sigma-Aldrich) polydimethylsiloxane (PDMS) in a 10:1 ratio of base agent to curing agent in a prefabricated mould. The PDMS solution was then temperature treated at 65 °C for 15 min and the reaction was allowed to continue for an additional 15 min at room temperature before the implants were removed from the mould. After fabrication, the moulds were placed in 100% ethanol to allow unreacted materials to leach out and sterilize the implants before storing them in sterile containers.

Implant preparation

The implants were sterilized in Betadine Surgical Scrub Veterinary solution (Avrio Health) for 12 h at 4 °C before surgery. For ADM coverage of the implant, a 1 cm × 1 cm square of ADM was placed covering the converse surface of the implant. Three equally spaced simple interrupted Monocryl monofilament 4-0 sutures (Ethicon) were used to anchor the ADM to the implant at the implant–ADM interface.

Hydrogel preparation

The hydrogel was formulated as previously described[89]. Briefly, the hydrogel was formulated with final concentrations of 2 wt% hydroxypropylmethylcellulose (HPMC)-C_{12} and 10 wt% poly(ethylene glycol)-block-poly(lactic acid) (PEG-PLA) nanoparticles (NPs). HPMC-C_{12} was synthesized as previously described, dissolved in PBS at 6 wt% and loaded into a 1-ml luer-lock syringe. A 20 wt% solution of NPs in PBS was diluted with additional PBS, or PBS containing recombinant osteopontin protein (SPP1) (R&D Systems) for a final dose of 15 µg per 100 µl and loaded into a separate 1-ml luer-lock syringe. The two syringes were connected with a female–female luer-lock elbow with care to avoid air at the interface of HPMC-C_{12} and the NP solution. The two solutions were mixed for 1 min or until a homogeneous hydrogel was formed. After mixing, the elbow was removed, a luer-lock cap was placed and the material was stored at 4 °C for up to 7 days before surgery.

In vitro release

Labelled recombinant osteopontin protein (SPP1) (R&D Systems) was made by reacting Alexa Fluor 647 (AF647) NHS ester (Lumiprobe) at 8× molar excess with SPP1. Briefly, 200 µg SPP1 was dissolved in 200 µl PBS, and 22 µl of AF647 NHS ester at 2.44 mg ml^{-1} was added dropwise with stirring. After 4 h at room temperature, 750 µl PBS was added to quench the reaction and the solution was spin filtered (Amicon 0.5 ml, 10 K MWCO) with PBS rinses until flowthrough had no more visible dye. SPP1-AF647 was concentrated to 1 mg ml^{-1} and incorporated into hydrogel at 15 µg per 100 µl for the in vitro release assay. Glass capillary tubes were cut to 4 inches, sealed on one end with epoxy and allowed to cure for at least 24 h. Hydrogel (100 µl) was injected into the bottom of each tube ($n = 3$), 400 µl PBS was injected on top carefully to not disrupt the gel surface, and tubes were sealed with parafilm and stored upright at 37 °C. At each time point, all 400 µl PBS was carefully removed from the tube and replaced with fresh PBS, avoiding disturbance of the gel surface. Samples were taken at 6, 14, 24 h and 2, 3, 5, 8, 12, 16, 19, 28 days, and fluorescence at 647 nm was measured using a Synergy H1 plate reader (BioTek). At the end of the study, gel was collected from the tubes, diluted with PBS, and the remaining AF647-SPP1 was quantified. Data are presented as AF647-SPP1 remaining in gel, calculated as $1 - M_t/M_\infty$, where M_t is the accumulative amount released at each time point and M_∞ is the total amount loaded in the gel at the beginning of the assay. Data were fit with a one-phase decay in GraphPad Prism and the half-life of release was determined.

Implant placement

For dorsal implant insertion, anaesthesia was induced and maintained with 1–3% isoflurane at a flow rate of 2 l min^{-1}. Adequate anaesthesia was confirmed with loss of hind-limb reflex to nociceptive stimuli. The dorsal skin was shaved and sterilized with Betadine Surgical Scrub Veterinary solution (Avrio Health), followed by sterile alcohol prep pads (FisherScientific). Next, a transverse incision was made through the panniculus carnosus on the medial aspect of the left mid-back with sterile scissors and forceps. A 2 cm × 2 cm subcutaneous pocket was raised caudally and laterally, large enough to fit the implant. A PDMS implant alone or PDMS implant covered with ADM was then placed in the subcutaneous pocket. Mice were divided into different experimental groups, each receiving one implant. For mice that received the ADM alone, a 1 × 1 cm square of ADM was placed in the subcutaneous pocket. The wound was closed without tension using 6 interrupted nylon monofilament 4-0 sutures (Dynarex). The incision was dressed using Krazyglue (Elmer's Products). Incisions were inspected daily.

For mice that received the hydrogel with recombinant SPP1, 100 µl of the gel suspension was injected adjacent to the implant once the incision was closed and glued.

For mice that received the recombinant SPP1 PBS injections, 10 µl of 50 ng µl^{-1} SPP1 resuspended in sterile PBS were injected subcutaneously over the top of the implant as well as adjacent to the implant (for a total of 20 µl) every other day for 28 days. The dosage of SPP1 was calculated on the basis of the release curve of SPP1 established through the in vitro release experiment, which demonstrated that 0.5 µg of SPP1 was released per day. We paralleled this amount by injecting 1 µg of SPP1 every other day.

Mice were hydrated with 1 ml of PBS at the end of the procedure.

Mouse FBR model collection

On POD 28, the capsule surrounding the implant was collected with dissecting scissors under ×2.5 Loupe magnification and processed for subsequent analysis. Mice were euthanized by carbon dioxide (CO_2) narcosis and cervical dislocation. The superior surface of the capsule was meticulously dissected following the edge of the implant, with overlying skin intact. Collected capsule was sent for histology. In addition, capsule used for FACS was removed from the overlying skin using ×2.5 Loupe magnification and mechanically digested using dissecting scissors to finely mince each specimen. Collected capsules for use in histology and IF staining were placed in tissue embedding cassettes.

Tensile testing (human samples)

Capsule specimens obtained from patients (Native capsule and ADM capsule) were tested using an Instron 5565 utilizing a 100-N load cell ($n = 6$). The capsule was excised with sharp surgical scissors as above and carefully cut into tapered 4 mm × 15 mm pieces. Tissue pieces were subsequently anchored between grips. The tissue was slowly separated (1% increase per second) until failure (defined by a clear drop in measured stress as tension increased). Young's modulus was determined by taking the slope of the linear portion of the stress–strain curve.

Tensile testing (ADM and PDMS)

ADM and PDMS samples were tested using an Instron 5565 utilizing a 100-N load cell. Materials were cut into tapered 5 mm × 10 mm pieces. Tissue pieces were subsequently anchored between grips. The tissue was slowly separated (1% increase per second) until failure (defined by a clear drop in measured stress as tension increased). Young's modulus

was determined by taking the slope of the linear portion of the stress–strain curve.

Tissue fixation (human and mouse samples)

Mouse capsule specimens were fixed in 4% paraformaldehyde solution in PBS for 24 h at 4 °C ($n = 3$ per condition). All human samples were fixed in 10% neutral buffered formalin (Thermo Fisher) for 24 h at room temperature ($n = 10$).

Materials and initial processing for all staining

Haematoxylin and eosin (H-3502, Vector Laboratories), Masson's trichrome (ab150686, Abcam), picrosirius red (ab150681, Abcam) and modified Verhoeff van Gieson's stain (Abcam) with standard protocols were used.

Immunofluorescence staining

Immunofluorescence staining was performed as previously described[46,108].

Haematoxylin and eosin staining

H&E staining was performed as described by the manufacturer (Sigma-Aldrich).

Insets for H&E staining were established by measuring capsule thickness across a given sample, determining the average thickness and selecting the region to magnify for the inset ($n = 6$).

Elastin stain

Verhoeff van Gieson staining was performed (Abcam) as described by the manufacturer. Normalized elastin density via van Gieson staining was determined by staining ADM alone with van Gieson's stain, calculating the mean pixel density of elastin staining for ADM alone and dividing each individual value obtained for ADM capsule and Native capsule pixel density by this mean.

Masson's trichrome stain

Trichrome staining was performed as described by the manufacturer (Abcam). Insets for Masson's trichrome figures were established by measuring collagen density across a given sample, determining the average collagen density and selecting the region to magnify for the inset ($n = 6$).

Picrosirius red staining and histologic analysis

Picrosirius red staining was performed as described by the manufacturer (Abcam), and histologic analysis using an image-processing algorithm was performed as previously described[47].

Luminex multiple immunoassay for Native and ADM capsule cytokine analysis (human samples)

Freshly collected human capsule specimens were collected from the operating room and placed on ice. The tissue was then minced and placed in liquid nitrogen. Protein isolation was then performed following the tissue homogenate protocol (MAN0017834, Thermo Fisher) using the recommended cell lysis buffer (Thermo Fisher, EPX-99999-000). Protein concentration was measured using the bicinchoninic acid method (Thermo Fisher). The 62-plex Luminex assay (custom built by eBioscience) to assess tissue cytokine content was conducted following manufacturer protocol. Two biological replicates were analysed per patient specimen.

Tissue preparation, FACS, multiplexing and scRNA-seq for human Native and ADM capsules

Capsule tissue from human specimens were prepared and isolated cells sorted via FACS as previously described ($n = 6$ per condition)[46]. Individual human native and ADM capsule dissociated tissue cellular suspensions were tagged with hashtag oligonucleotides (HTOs) following manufacturer protocol and then pooled. Quality control and scRNA-seq were performed on sorted cells using the 10× Chromium Single Cell platform (Single Cell 3' v.3, 10x Genomics) at the Stanford Functional Genomics Facility (SFGF), Stanford University, Palo Alto.

Data processing, fastq generation and read mapping (human samples)

Base calls were converted to reads with the software Cell Ranger's (10× Genomics, v.3.1) implementation 'mkfastq'. These were then aligned against the GRCh38 v.3.0.0 (for human) genome using Cell Ranger's count function (an implementation of STAR v.2.7.0) with SC3Pv3 chemistry and 5,000 expected cells per sample[109]. Cell barcodes representative of quality cells were delineated from barcodes of apoptotic cells or background RNA on the basis of a threshold of having at least 200 transcripts profiled and less than 10% of their transcriptome of mitochondrial origin.

Data normalization, hashtag oligo demultiplexing and cell subpopulation identification (human samples)

Unique molecular identifiers (UMIs) from each cell barcode were retained for all downstream analysis. Raw UMI counts were normalized with a scale factor of 10,000 UMIs per cell and subsequently natural log transformed with a pseudocount of 1 using the R package Seurat (v.4.0.5)[110]. DNA hashtag oligonucleotides (HTOs) for human samples were demultiplexed using Seurat's implementation 'HTODemux'. Briefly, *k*-medoid clustering was performed on the normalized HTO values, after which a 'negative' HTO distribution was calculated. For each HTO, the cluster with the lowest average value was treated as the negative group and a negative binomial distribution was fit to this cluster. Using the 0.99 quantile of this distribution as a threshold, each cell was classified as positive or negative for each HTO. Cells that were positive for more than one HTO were annotated as doublets and removed. Cells that were not positive for any HTO were also removed. Aggregated data were then evaluated using UMAP analysis over the first 15 principal components[111].

We chose Louvain-based clustering analysis for our scRNA-seq data as it is the most used graph-based clustering method for scRNA-seq data and is used to assist users in identifying different cell types or cell subpopulations within a given dataset. It is commonly used in part due to its scalability for large scRNA-seq analysis datasets. Further, we made use of Seurat for our scRNA-seq analyses, which applies the Louvain algorithm as the default clustering method[112].

Cell annotations were assigned using SingleR (v.3.11) against the Blueprint + ENCODE reference database for human cells.

Generation of characteristic subpopulation markers and enrichment analysis (human samples)

Cell-type marker lists were generated using two separate approaches. In the first approach, we employed Seurat's native FindMarkers function with a log fold-change threshold of 0.25 using the receiver operating characteristic (ROC) test to assign predictive power to each gene. However, to better account for the mutual information contained within highly correlated predictive genes, we also employed a characteristic direction analysis[113]. The 100 most highly ranked genes from this analysis for each cluster were used to perform gene set enrichment analysis against the BROAD Institute databases (http://software.broadinstitute.org/gsea/index.jsp) in a programmatic fashion using EnrichR (v.2.1)[51]. To identify differences in gene expression between ADM and Native capsule monocytes/macrophages, a Wilcoxon rank-sum test was implemented in Seurat.

Tissue preparation, dissociation and scRNA-seq of mouse Native and ADM capsules

Mouse capsules were collected at POD 28. Capsules were processed as previously described[46,114]. Quality control and scRNA-seq were

performed on unsorted cells using the 10x Chromium Single Cell platform (Single Cell 3′ v.3, 10x Genomics) at the SFGF.

Data processing, fastq generation and read mapping (mouse samples)

Base calls were converted to reads using the Cell Ranger (10x Genomics, v.3.1) implementation 'mkfastq' and then aligned against the Cell Ranger mm10 reference genome using Cell Ranger's count function with SC3Pv3 chemistry and 5,000 expected cells per sample, as previously described[46]. For mouse datasets, a maximum percent mitochondrial RNA cut-off of 15%, 7,500 maximum unique genes and 85,000 maximum RNA counts were used.

Data normalization and cell subpopulation identification (mouse samples)

UMIs from each cell barcode were retained for all downstream analysis, normalized with a scale factor of 10,000 UMIs per cell and subsequently natural log transformed with a pseudocount of 1 using the R package Seurat (v.4.0.5)[51]. The first 15 principal components of the aggregated data were then used for UMAP analysis[115].

Cell annotations were assigned using SingleR (v.3.11) against the mouse RNA-seq reference dataset available at https://rdrr.io/github/dviraran/SingleR/man/mouse.rnaseq.html. Cell-type marker lists were generated using Seurat's native 'FindMarkers' function with a log fold-change threshold of 0.25, using the ROC test to assign predictive power to each gene. The 200 most highly ranked genes from this analysis for each cluster were used to perform gene set enrichment analysis in a programmatic fashion using EnrichR (v.2.1)[51]. For integration of human and mouse scRNA-seq datasets, integrated cross-species analyses were performed using orthologue mapping via Seurat's label transfer approach, as previously described[110].

CellChat receptor–ligand analysis

To evaluate the potential for interactions between different cell types in our dataset, we applied the recently developed CellChat platform[58]. This was implemented using our scRNA-seq Seurat object in R, in conjunction with the standalone CellChat Shiny App for its Cell–Cell Communication Atlas Explorer. Cells were binned according to the SingleR-defined cell type classifications. Default parameterizations were used throughout, and secreted signalling, ECM–receptor and cell–cell contact relationships were considered.

CODEX spatial analysis

To spatially phenotype the human specimens, we used Co-Detection by Indexing (CODEX), an assay in which markers are labelled with oligonucleotide-conjugated antibodies and iteratively imaged between cyclic additions and washouts of dye-labelled oligonucleotides. A custom CODEX panel was designed to assess capsule cells within the tissue (Table 2).

Using a CODEX-integrated Keyence BZ-X instrument (Akoya Biosciences) image acquisition was then performed. Using software from Akoya Biosciences, the raw images were processed, with cell segmentation and rendering. Cell segmentation (Voronoi-based) was performed using default platform settings, so that all downstream cell-level analyses were conducted on the basis of protein expression within the boundaries of individual cells.

The CODEX was visualized using Akoya Biosciences Multiplex Analysis Viewer (MAV) in ImageJ. The resulting .fcs files were then concatenated in FlowJo and imported into the Monocle3 (v.1.3.6) and STvEA (v.0.2.0) R packages for further analysis. After debris removal, the processed UMAP manifold was analysed through Monocle3 with a post-manifold threshold of >10,000 cells per cluster. Analysis of the protein staining patterns was then used to assign cell types. The cell interactions were then inferred using STvEA for cell types at >2.5% of total abundance at $k = 20$ nearest neighbours to quantify cell spatial interactions, and differential interaction maps were generated using graph scores.

Statistical methods

Statistical testing was performed in GraphPad Prism v.9 unless otherwise stated. For two-group comparisons, unpaired *t*-test was used. For multigroup analysis, one-way analysis of variance (ANOVA) with Bonferroni's post hoc correction was used to compare groups; $P < 0.05$ conferred statistical significance for all tests.

Reporting summary

Further information on research design is available in the Nature Portfolio Reporting Summary linked to this article.

Data availability

The scRNA-seq data generated during the study are available from the GEO repository (GSE: GSE279258). Original scripts for the ECM ultrastructure algorithm are available on Github at https://github.com/shamikmascharak/Mascharak-et-al-ENF (ref. 116). The raw and analysed datasets generated during the study are available for research purposes from the corresponding authors on reasonable request.

References

1. Major, M. R., Wong, V. W., Nelson, E. R., Longaker, M. T. & Gurtner, G. C. The foreign body response: at the interface of surgery and bioengineering. *Plast. Reconstr. Surg.* **135**, 1489–1498 (2015).
2. Parker, J. B., Griffin, M. F., Spielman, A. F., Wan, D. C. & Longaker, M. T. Exploring the overlooked roles and mechanisms of fibroblasts in the foreign body response. *Adv. Wound Care* **12**, 85–96 (2023).
3. Anderson, J. M., Rodriguez, A. & Chang, D. T. Foreign body reaction to biomaterials. *Semin. Immunol.* **20**, 86–100 (2008).
4. Gibon, E. et al. The biological response to orthopedic implants for joint replacement. II: Polyethylene, ceramics, PMMA, and the foreign body reaction. *J. Biomed. Mater. Res. B* **105**, 1685–1691 (2017).
5. Carnicer-Lombarte, A., Chen, S. T., Malliaras, G. G. & Barone, D. G. Foreign body reaction to implanted biomaterials and its impact in nerve neuroprosthetics. *Front. Bioeng. Biotechnol.* **9**, 622524 (2021).
6. Sivaraj, D. et al. IQGAP1-mediated mechanical signaling promotes the foreign body response to biomedical implants. *FASEB J.* **36**, e22007 (2022).
7. Arya, R. K., Goswami, R. & Rahaman, S. O. Mechanotransduction via a TRPV4-Rac1 signaling axis plays a role in multinucleated giant cell formation. *J. Biol. Chem.* **296**, 100129 (2021).
8. Noskovicova, N. et al. Suppression of the fibrotic encapsulation of silicone implants by inhibiting the mechanical activation of pro-fibrotic TGF-beta. *Nat. Biomed. Eng.* **5**, 1437–1456 (2021).
9. Ni, Y. et al. Macrophages modulate stiffness-related foreign body responses through plasma membrane deformation. *Proc. Natl Acad. Sci. USA* **120**, e2213837120 (2023).
10. Doloff, J. C. et al. The surface topography of silicone breast implants mediates the foreign body response in mice, rabbits and humans. *Nat. Biomed. Eng.* **5**, 1115–1130 (2021).
11. Chandorkar, Y., K, R. & Basu, B. The foreign body response demystified. *ACS Biomater. Sci. Eng.* **5**, 19–44 (2019).
12. Basu, C. B., Leong, M. & Hicks, M. J. Acellular cadaveric dermis decreases the inflammatory response in capsule formation in reconstructive breast surgery. *Plast. Reconstr. Surg.* **126**, 1842–1847 (2010).
13. Liang, N. E. et al. Attenuating chronic fibrosis: decreasing foreign body response with acellular dermal matrix. *Tissue Eng. B* **29**, 671–680 (2023).

14. Carruthers, C. A. et al. Histologic characterization of acellular dermal matrices in a porcine model of tissue expander breast reconstruction. *Tissue Eng. A* **21**, 35–44 (2015).
15. Chien, P. N. et al. In vivo comparison of three human acellular dermal matrices for breast reconstruction. *Vivo* **35**, 2719–2728 (2021).
16. Lee, J. S. et al. Influence of irradiation on capsules of silicone implants covered with acellular dermal matrix in mice. *Aesthetic Plast. Surg.* **46**, 937–946 (2022).
17. Woo, S. H. et al. Comparison of the effects of acellular dermal matrix and montelukast on radiation-induced peri-implant capsular formation in rabbits. *Ann. Plast. Surg.* **85**, 299–305 (2020).
18. Kim, I. K., Park, S. O., Chang, H. & Jin, U. S. Inhibition mechanism of acellular dermal matrix on capsule formation in expander-implant breast reconstruction after postmastectomy radiotherapy. *Ann. Surg. Oncol.* **25**, 2279–2287 (2018).
19. Chopra, K. et al. Acellular dermal matrix reduces capsule formation in two-stage breast reconstruction. *Int. Wound J.* **14**, 414–419 (2017).
20. Breuing, K. H. & Warren, S. M. Immediate bilateral breast reconstruction with implants and inferolateral AlloDerm slings. *Ann. Plast. Surg.* **55**, 232–239 (2005).
21. Spear, S. L., Seruya, M., Clemens, M. W., Teitelbaum, S. & Nahabedian, M. Y. Acellular dermal matrix for the treatment and prevention of implant-associated breast deformities. *Plast. Reconstr. Surg.* **127**, 1047–1058 (2011).
22. Cheng, A., Lakhiani, C. & Saint-Cyr, M. Treatment of capsular contracture using complete implant coverage by acellular dermal matrix: a novel technique. *Plast. Reconstr. Surg.* **132**, 519–529 (2013).
23. Gabriel, A. & Maxwell, G. P. AlloDerm RTU integration and clinical outcomes when used for reconstructive breast surgery. *Plast. Reconstr. Surg. Glob. Open* **6**, e1744 (2018).
24. Kuehlmann, B., Burkhardt, R., Kosaric, N. & Prantl, L. Capsular fibrosis in aesthetic and reconstructive-cancer patients: a retrospective analysis of 319 cases. *Clin. Hemorheol. Microcirc.* **70**, 191–200 (2018).
25. Jones, G. et al. Prepectoral immediate direct-to-implant breast reconstruction with anterior alloderm coverage. *Plast. Reconstr. Surg.* **140**, 31s–38s (2017).
26. Lardi, A. M., Ho-Asjoe, M., Junge, K. & Farhadi, J. Capsular contracture in implant based breast reconstruction–the effect of porcine acellular dermal matrix. *Gland Surg.* **6**, 49–56 (2017).
27. Namnoum, J. D. & Moyer, H. R. The role of acellular dermal matrix in the treatment of capsular contracture. *Clin. Plast. Surg.* **39**, 127–136 (2012).
28. Baker, B. G. et al. A prospective comparison of short-term outcomes of subpectoral and prepectoral strattice-based immediate breast reconstruction. *Plast. Reconstr. Surg.* **141**, 1077–1084 (2018).
29. Salzberg, C. A., Ashikari, A. Y., Berry, C. & Hunsicker, L. M. Acellular dermal matrix-assisted direct-to-implant breast reconstruction and capsular contracture: a 13-year experience. *Plast. Reconstr. Surg.* **138**, 329–337 (2016).
30. Wan, D. & Rohrich, R. J. Revisiting the management of capsular contracture in breast augmentation: a systematic review. *Plast. Reconstr. Surg.* **137**, 826–841 (2016).
31. Macadam, S. A. & Lennox, P. A. Acellular dermal matrices: use in reconstructive and aesthetic breast surgery. *Can. J. Plast. Surg.* **20**, 75–89 (2012).
32. Fagerberg, L. et al. Analysis of the human tissue-specific expression by genome-wide integration of transcriptomics and antibody-based proteomics. *Mol. Cell. Proteomics* **13**, 397–406 (2014).
33. Si, J., Wang, C., Zhang, D., Wang, B. & Zhou, Y. Osteopontin in bone metabolism and bone diseases. *Med. Sci. Monit.* **26**, e919159 (2020).
34. Rittling, S. R. & Singh, R. Osteopontin in immune-mediated diseases. *J. Dent. Res.* **94**, 1638–1645 (2015).
35. Morse, C. et al. Proliferating SPP1/MERTK-expressing macrophages in idiopathic pulmonary fibrosis. *Eur. Respir. J.* **54**, 1802441 (2019).
36. Song, Z. et al. Osteopontin takes center stage in chronic liver disease. *Hepatology* **73**, 1594–1608 (2021).
37. Liu, W. et al. Deciphering key foreign body reaction-related transcription factors and genes through transcriptome analysis. *Front. Mol. Biosci.* **9**, 843391 (2022).
38. Tsai, A. T. et al. The role of osteopontin in foreign body giant cell formation. *Biomaterials* **26**, 5835–5843 (2005).
39. Wei, T. et al. The significance of secreted phosphoprotein 1 in multiple human cancers. *Front. Mol. Biosci.* **7**, 565383 (2020).
40. Han, H. et al. Macrophage-derived osteopontin (SPP1) protects from nonalcoholic steatohepatitis. *Gastroenterology* **165**, 201–217 (2023).
41. Uaesoontrachoon, K. et al. Osteopontin and skeletal muscle myoblasts: association with muscle regeneration and regulation of myoblast function in vitro. *Int. J. Biochem. Cell Biol.* **40**, 2303–2314 (2008).
42. Wang, X. et al. Signalling by senescent melanocytes hyperactivates hair growth. *Nature* **618**, 808–817 (2023).
43. Padmanabhan, J. et al. Allometrically scaling tissue forces drive pathological foreign-body responses to implants via Rac2-activated myeloid cells. *Nat. Biomed. Eng.* **7**, 1419–1436 (2023).
44. Baumann, L. et al. Clinical relevance of elastin in the structure and function of skin. *Aesthet. Surg. J. Open Forum* **3**, ojab019 (2021).
45. Wang, K., Meng, X. & Guo, Z. Elastin structure, synthesis, regulatory mechanism and relationship with cardiovascular diseases. *Front. Cell Dev. Biol.* **9**, 596702 (2021).
46. Mascharak, S. et al. Multi-omic analysis reveals divergent molecular events in scarring and regenerative wound healing. *Cell Stem Cell* **29**, 315–327.e6 (2022).
47. Mascharak, S. et al. Desmoplastic stromal signatures predict patient outcomes in pancreatic ductal adenocarcinoma. *Cell Rep. Med.* **4**, 101248 (2023).
48. Chen, K. et al. Disrupting mechanotransduction decreases fibrosis and contracture in split-thickness skin grafting. *Sci. Transl. Med.* **14**, ARTN eabj9152 (2022).
49. Ridiandries, A., Tan, J. T. M. & Bursill, C. A. The role of chemokines in wound healing. *Int. J. Mol. Sci.* **19**, ARTN 3217 (2018).
50. Gibbs, S., Spiekstra, S. W., Breetveld, M., Rustemeyer, T. & Scheper, R. J. Wound healing factors secreted by epidermal keratinocytes and dermal fibroblasts in skin substitutes. *Wound Repair Regen.* **15**, 708–717 (2007).
51. Chen, E. Y. et al. Enrichr: interactive and collaborative HTML5 gene list enrichment analysis tool. *BMC Bioinformatics* **14**, 128 (2013).
52. Depuydt, M. A. C. et al. Microanatomy of the human atherosclerotic plaque by single-cell transcriptomics. *Circ. Res.* **127**, 1437–1455 (2020).
53. Wen, Y., Yan, H. R., Wang, B. & Liu, B. C. Macrophage heterogeneity in kidney injury and fibrosis. *Front. Immunol.* **12**, 681748 (2021).
54. Sauler, M. et al. Characterization of the COPD alveolar niche using single-cell RNA sequencing. *Nat. Commun.* **13**, 494 (2022).
55. Luo, Z. et al. Hypoxia signaling in human health and diseases: implications and prospects for therapeutics. *Signal Transduct. Target. Ther.* **7**, 218 (2022).
56. Schmitt-Grohe, S. et al. Lipopolysaccharide binding protein, cytokine production in whole blood, and lipoproteins in cystic fibrosis. *Pediatr. Res.* **58**, 903–907 (2005).

57. Gaudet, R. G. et al. A human apolipoprotein L with detergent-like activity kills intracellular pathogens. *Science* **373**, eabf8113 (2021).
58. Jin, S. et al. Inference and analysis of cell–cell communication using CellChat. *Nat. Commun.* **12**, 1088 (2021).
59. Shirakawa, K. & Sano, M. Osteopontin in cardiovascular diseases. *Biomolecules* **11**, 1047 (2021).
60. Liu, Y. et al. Immune phenotypic linkage between colorectal cancer and liver metastasis. *Cancer Cell* **40**, 424–437.e5 (2022).
61. Komori, T. Regulation of bone development and extracellular matrix protein genes by RUNX2. *Cell Tissue Res.* **339**, 189–195 (2010).
62. Sheikh, Z., Brooks, P. J., Barzilay, O., Fine, N. & Glogauer, M. Macrophages, foreign body giant cells and their response to implantable biomaterials. *Materials* **8**, 5671–5701 (2015).
63. Lazarov, T., Juarez-Carreno, S., Cox, N. & Geissmann, F. Physiology and diseases of tissue-resident macrophages. *Nature* **618**, 698–707 (2023).
64. Schreib, C. C. et al. Lipid deposition profiles influence foreign body responses. *Adv. Mater.* **35**, e2205709 (2023).
65. Black, S. et al. CODEX multiplexed tissue imaging with DNA-conjugated antibodies. *Nat. Protoc.* **16**, 3802–3835 (2021).
66. Griffin, M. F. et al. Piezo inhibition prevents and rescues scarring by targeting the adipocyte to fibroblast transition. Preprint at *bioRxiv* https://doi.org/10.1101/2023.04.03.535302 (2023).
67. Safran, T. et al. Current concepts in capsular contracture: pathophysiology, prevention, and management. *Semin. Plast. Surg.* **35**, 189–197 (2021).
68. Parlani, M., Bedell, M. L., Mikos, A. G., Friedl, P. & Dondossola, E. Dissecting the recruitment and self-organization of alphaSMA-positive fibroblasts in the foreign body response. *Sci. Adv.* **8**, eadd0014 (2022).
69. Zhang, T. et al. NUAK1 promotes organ fibrosis via YAP and TGF-beta/SMAD signaling. *Sci. Transl. Med.* **14**, eaaz4028 (2022).
70. Du, W., Tang, Z., Yang, F., Liu, X. & Dong, J. Icariin attenuates bleomycin-induced pulmonary fibrosis by targeting Hippo/YAP pathway. *Biomed. Pharmacother.* **143**, 112152 (2021).
71. Garoffolo, G. et al. Reduction of cardiac fibrosis by interference with YAP-dependent transactivation. *Circ. Res.* **131**, 239–257 (2022).
72. Mascharak, S. et al. Preventing Engrailed-1 activation in fibroblasts yields wound regeneration without scarring. *Science* **372**, eaba2374 (2021).
73. Meli, V. S. et al. YAP-mediated mechanotransduction tunes the macrophage inflammatory response. *Sci. Adv.* **6**, eabb8471 (2020).
74. Chen, L., Jin, X., Ma, J., Xiang, B. & Li, X. YAP at the progression of inflammation. *Front. Cell Dev. Biol.* **11**, 1204033 (2023).
75. Katzel, E. B. et al. A novel animal model for studying silicone gel-related capsular contracture. *Plast. Reconstr. Surg.* **126**, 1483–1491 (2010).
76. Lin, A. J. et al. In search of a murine model of radiation-induced periprosthetic capsular fibrosis. *Ann. Plast. Surg.* **80**, S204–S210 (2018).
77. Mack, M. Inflammation and fibrosis. *Matrix Biol.* **68-69**, 106–121 (2018).
78. Duscher, D. et al. Mechanotransduction and fibrosis. *J. Biomech.* **47**, 1997–2005 (2014).
79. Duong, L. T. & Rodan, G. A. PYK2 is an adhesion kinase in macrophages, localized in podosomes and activated by beta(2)-integrin ligation. *Cell Motil. Cytoskeleton* **47**, 174–188 (2000).
80. DeFife, K. M., Jenney, C. R., Colton, E. & Anderson, J. M. Cytoskeletal and adhesive structural polarizations accompany IL-13-induced human macrophage fusion. *J. Histochem. Cytochem.* **47**, 65–74 (1999).
81. Goffin, J. M. et al. Focal adhesion size controls tension-dependent recruitment of alpha-smooth muscle actin to stress fibers. *J. Cell Biol.* **172**, 259–268 (2006).
82. Cai, P. et al. VEGF signaling governs the initiation of biliary-mediated liver regeneration through the PI3K-mTORC1 axis. *Cell Rep.* **42**, 113028 (2023).
83. Engelbrecht, E., Kooistra, T. & Knipe, R. S. The vasculature in pulmonary fibrosis. *Curr. Tissue Microenviron. Rep.* **3**, 83–97 (2022).
84. Huang, C. & Ogawa, R. The vascular involvement in soft tissue fibrosis—lessons learned from pathological scarring. *Int. J. Mol. Sci.* **21**, 2542 (2020).
85. Liaw, L. et al. Altered wound healing in mice lacking a functional osteopontin gene (spp1). *J. Clin. Invest.* **101**, 1468–1478 (1998).
86. Appel, E. A. et al. Self-assembled hydrogels utilizing polymer-nanoparticle interactions. *Nat. Commun.* **6**, 6295 (2015).
87. Stapleton, L. M. et al. Dynamic hydrogels for prevention of post-operative peritoneal adhesions. *Adv. Ther.* **4**, ARTN 2000242 (2021).
88. Stapleton, L. M. et al. Use of a supramolecular polymeric hydrogel as an effective post-operative pericardial adhesion barrier. *Nat. Biomed. Eng.* **3**, 611–620 (2019).
89. Meany, E. L. et al. Injectable polymer-nanoparticle hydrogel for the sustained intravitreal delivery of bimatoprost. *Adv. Ther.* https://doi.org/10.1002/adtp.202200207 (2023).
90. Roth, G. A. et al. Injectable hydrogels for sustained codelivery of subunit vaccines enhance humoral immunity. *ACS Cent. Sc.i* **6**, 1800–1812 (2020).
91. Gale, E. C. et al. Hydrogel-based slow release of a receptor-binding domain subunit vaccine elicits neutralizing antibody responses against SARS-CoV-2. *Adv. Mater.* **33**, e2104362 (2021).
92. Grosskopf, A. K. et al. Delivery of CAR-T cells in a transient injectable stimulatory hydrogel niche improves treatment of solid tumors. *Sci. Adv.* **8**, eabn8264 (2022).
93. Kasse, C. M. et al. Subcutaneous delivery of an antibody against SARS-CoV-2 from a supramolecular hydrogel depot. *Biomater. Sci.* **11**, 2065–2079 (2023).
94. d'Aquino, A. I. et al. Sustained delivery of GLP-1 receptor agonists from injectable biomimetic hydrogels improves treatment of diabetes. Preprint at *bioRxiv* https://doi.org/10.1101/2023.01.28.526057 (2023).
95. Miletti-Gonzalez, K. E. et al. Identification of function for CD44 intracytoplasmic domain (CD44-ICD): modulation of matrix metalloproteinase 9 (MMP-9) transcription via novel promoter response element. *J. Biol. Chem.* **287**, 18995–19007 (2012).
96. Qian, J. et al. Cancer-associated mesothelial cells promote ovarian cancer chemoresistance through paracrine osteopontin signaling. *J. Clin. Invest.* **131**, e146186 (2021).
97. Doloff, J. C. et al. Colony stimulating factor-1 receptor is a central component of the foreign body response to biomaterial implants in rodents and non-human primates. *Nat. Mater.* **16**, 671–680 (2017).
98. Zanotti, S. et al. Osteopontin is highly expressed in severely dystrophic muscle and seems to play a role in muscle regeneration and fibrosis. *Histopathology* **59**, 1215–1228 (2011).
99. Maeda, Y. et al. CXCL12 and osteopontin from bone marrow-derived mesenchymal stromal cells improve muscle regeneration. *Sci. Rep.* **7**, 3305 (2017).
100. Ghasemi, H. et al. Transitional cell carcinoma matrix stiffness regulates the osteopontin and YAP expression in recurrent patients. *Mol. Biol. Rep.* **48**, 4253–4262 (2021).
101. Dong, Y. et al. Higher matrix stiffness as an independent initiator triggers epithelial–mesenchymal transition and facilitates HCC metastasis. *J. Hematol. Oncol.* **12**, 112 (2019).

102. You, Y. et al. Higher matrix stiffness upregulates osteopontin expression in hepatocellular carcinoma cells mediated by integrin beta1/GSK3beta/beta-catenin signaling pathway. *PLoS ONE* **10**, e0134243 (2015).
103. Antonopoulos, A., North, S. J., Haslam, S. M. & Dell, A. Glycosylation of mouse and human immune cells: insights emerging from N-glycomics analyses. *Biochem. Soc. Trans.* **39**, 1334–1340 (2011).
104. Cobb, B. A. Is donor glycosylation the gatekeeper for xenotransplantation. *Am. J. Transplant.* **14**, 745–747 (2014).
105. Doll, S. & Burlingame, A. L. Mass spectrometry-based detection and assignment of protein posttranslational modifications. *ACS Chem. Biol.* **10**, 63–71 (2015).
106. Jaffe, E. S. et al. Best practices guideline for the pathologic diagnosis of breast implant-associated anaplastic large-cell lymphoma. *J. Clin. Oncol.* **38**, 1102–1111 (2020).
107. Hlady, V. V. & Buijs, J. Protein adsorption on solid surfaces. *Curr. Opin. Biotechnol.* **7**, 72–77 (1996).
108. Griffin, M. F. et al. JUN promotes hypertrophic skin scarring via CD36 in preclinical in vitro and in vivo models. *Sci. Transl. Med.* **13**, eabb3312 (2021).
109. Dobin, A. et al. STAR: ultrafast universal RNA-seq aligner. *Bioinformatics* **29**, 15–21 (2013).
110. Stuart, T. et al. Comprehensive integration of single-cell data. *Cell* **177**, 1888–1902.e21 (2019).
111. Becht, E. et al. Dimensionality reduction for visualizing single-cell data using UMAP. *Nat. Biotechnol.* **37**, 38–44 (2018).
112. Zhang, S., Li, X., Lin, J., Lin, Q. & Wong, K. C. Review of single-cell RNA-seq data clustering for cell-type identification and characterization. *RNA* **29**, 517–530 (2023).
113. Clark, N. R. et al. The characteristic direction: a geometrical approach to identify differentially expressed genes. *BMC Bioinformatics* **15**, 79 (2014).
114. Mack, K. K. et al. Allele-specific expression reveals genetic drivers of tissue regeneration in mice. *Cell Stem Cell* **30**, 1368–1381.e6 (2023).
115. Gulati, G. S. et al. Single-cell transcriptional diversity is a hallmark of developmental potential. *Science* **367**, 405–411 (2020).
116. Mascharak, S. Mascharak-et-al-ENF. *GitHub* https://github.com/shamikmascharak/Mascharak-et-al-ENF (2022).

Acknowledgements

We thank the Stanford Functional Genomics Facility, Stanford Cell Sciences Imaging Facility, and Stanford Shared FACS Facility Cores. M.T.L. discloses support for the research described in this study from the Hagey Laboratory for Pediatric Regenerative Medicine, the Gunn/Oliver Research Fund, the Stinehart/Reed Award, the Scleroderma Research Foundation, the Wu Tsai Human Performance Alliance, the Pitch and Catherine Johnson Fund, the National Institutes of Health (NIH; U24-DE029463, GM-136659, R01-GM116892, R01-DE027346, R01-AR081343, R01-DE032677). D.C.W. discloses support for the research described in this study from the Hagey Laboratory for Pediatric Regenerative Medicine, the NIH (U24-DE029463, R01-DE027346, R01-AR081343, R01-DE032677). G.C.G. discloses support for the research described in this study from the NIH (U24-DE029463). J.B.P. discloses support for the research described in this study from the California Institute for Regenerative Medicine (CIRM EDUC4-12782) and the Stanford Bio-X Graduate Fellowship Program. Schematics were created with BioRender.com.

Author contributions

M.F.G., J.B.P. and R.T. conceptualized the project. M.F.G., J.B.P., R.T. and N.E.L. conducted formal analysis. G.C.G., D.C.W. and M.T.L. acquired funding. M.F.G., J.B.P., R.T., N.E.L., C.V., A.M., M.K., M.D.J., E.L.M., J.L.G., D.H., R.S.N. and K.S. conducted investigations. M.F.G., J.B.P., R.T., N.E.L., E.L.M., J.L.G. and R.S.N. developed the methodology. M.F.G., J.B.P., R.T., N.E.L., J.L.G., D.H. and M.J. developed software. D.N., G.C.G., S.C.H., C.K.F.C., M.J., E.A.A., A.M., D.C.W. and M.T.L. supervised the project. M.F.G., J.B.P., R.T., N.E.L., C.V., M.K. and E.L.M. performed visualization. M.F.G., J.B.P., R.T. and N.E.L. wrote the original draft. R.T. and N.E.L. contributed equally to this paper. M.F.G., J.B.P., G.C.G., S.C.H., C.K.F.C., E.A.A., A.M., D.C.W. and M.T.L. reviewed and edited the paper.

Competing interests

The authors declare no competing interests.

Additional information

Extended data is available for this paper at https://doi.org/10.1038/s41551-025-01361-4.

Supplementary information The online version contains supplementary material available at https://doi.org/10.1038/s41551-025-01361-4.

Correspondence and requests for materials should be addressed to Arash Momeni, Derrick C. Wan or Michael T. Longaker.

Peer review information *Nature Biomedical Engineering* thanks Maksim Plikus and the other, anonymous, reviewer(s) for their contribution to the peer review of this work.

https://doi.org/10.1038/s41551-025-01361-4

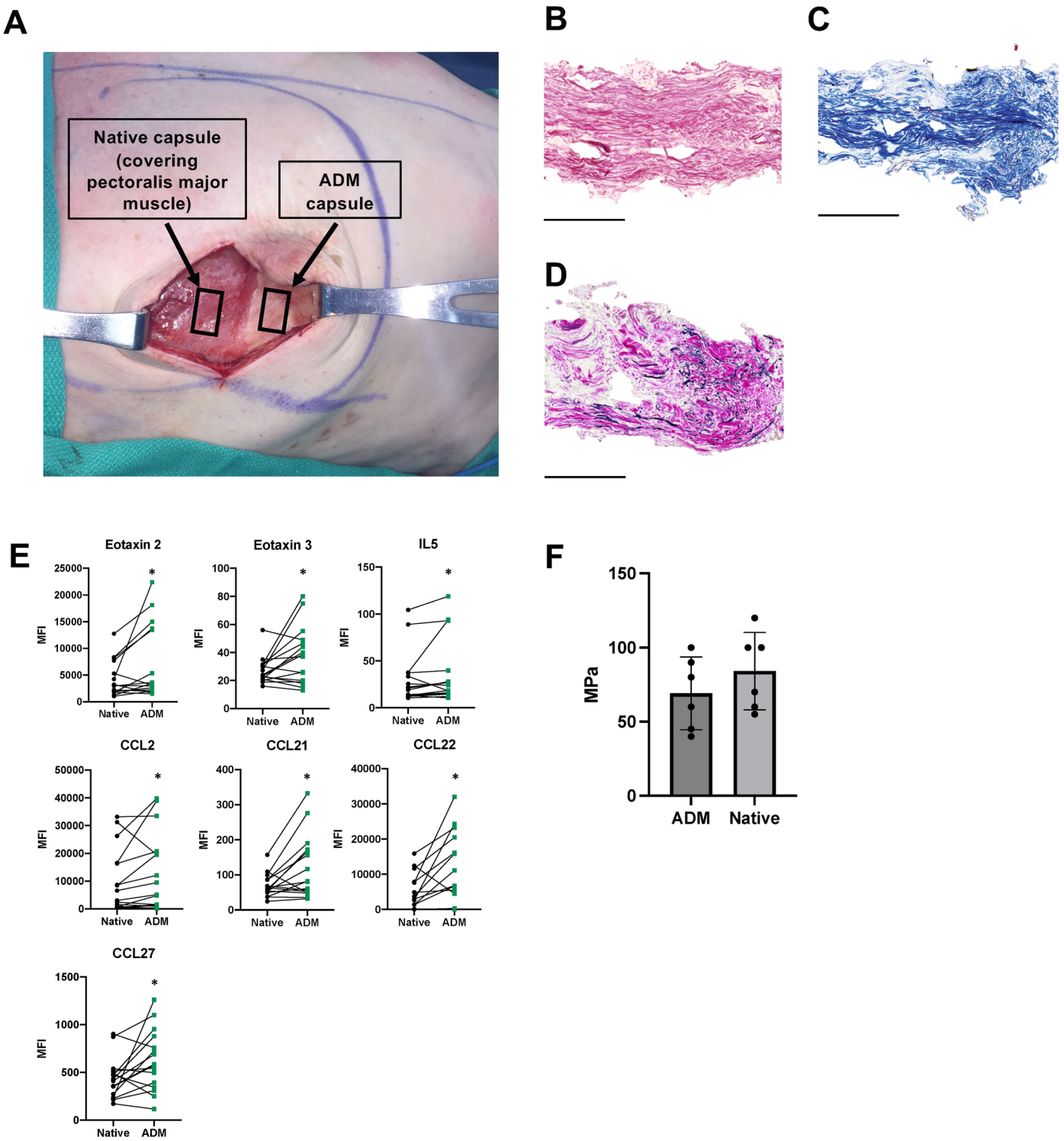

Extended Data Fig. 1 | Comparison of human capsule specimens with and without acellular dermal matrix (ADM). (**a**) Intraoperative photograph following breast implant removal showing acellular dermal matrix (ADM right) and Native capsule (left) retrieval (black arrows). (**b**) Hematoxylin and eosin (H&E) staining of ADM alone. (**c**) Trichrome staining of ADM alone. (**d**) Elastin staining of ADM alone. (**e**) Luminex secretion assay comparing median fluorescent intensity (MFI) of the following chemokine markers between implant alone (Native) and Acellular Dermal Matrix-coated (ADM) capsule: Eotaxin-2, Eotaxin-3, Interleukin 5 (IL-5), Chemokine ligand 2 (CCL2), Chemokine ligand 21 (CCL21), Chemokine ligand 22 (CCL22), and Chemokine ligand 27 (CCL27). Linked data points represent Native and ADM capsules retrieved from the same patient. (**f**) Tensile Young's modulus of ADM and Native capsule (n = 6); Statistical comparisons were made using an unpaired, two-tailed t-test. (**e**) Data shown as absolute values (**f**) Data shown as mean modulus of elasticity (MPa) ± standard deviation (S.D.); Statistical comparisons were made using an unpaired, two-tailed t-test. *$P < 0.05$. (**b**–**d**) Scale bars 600 μm. n = 10 human specimens unless otherwise specified.

https://doi.org/10.1038/s41551-025-01361-4

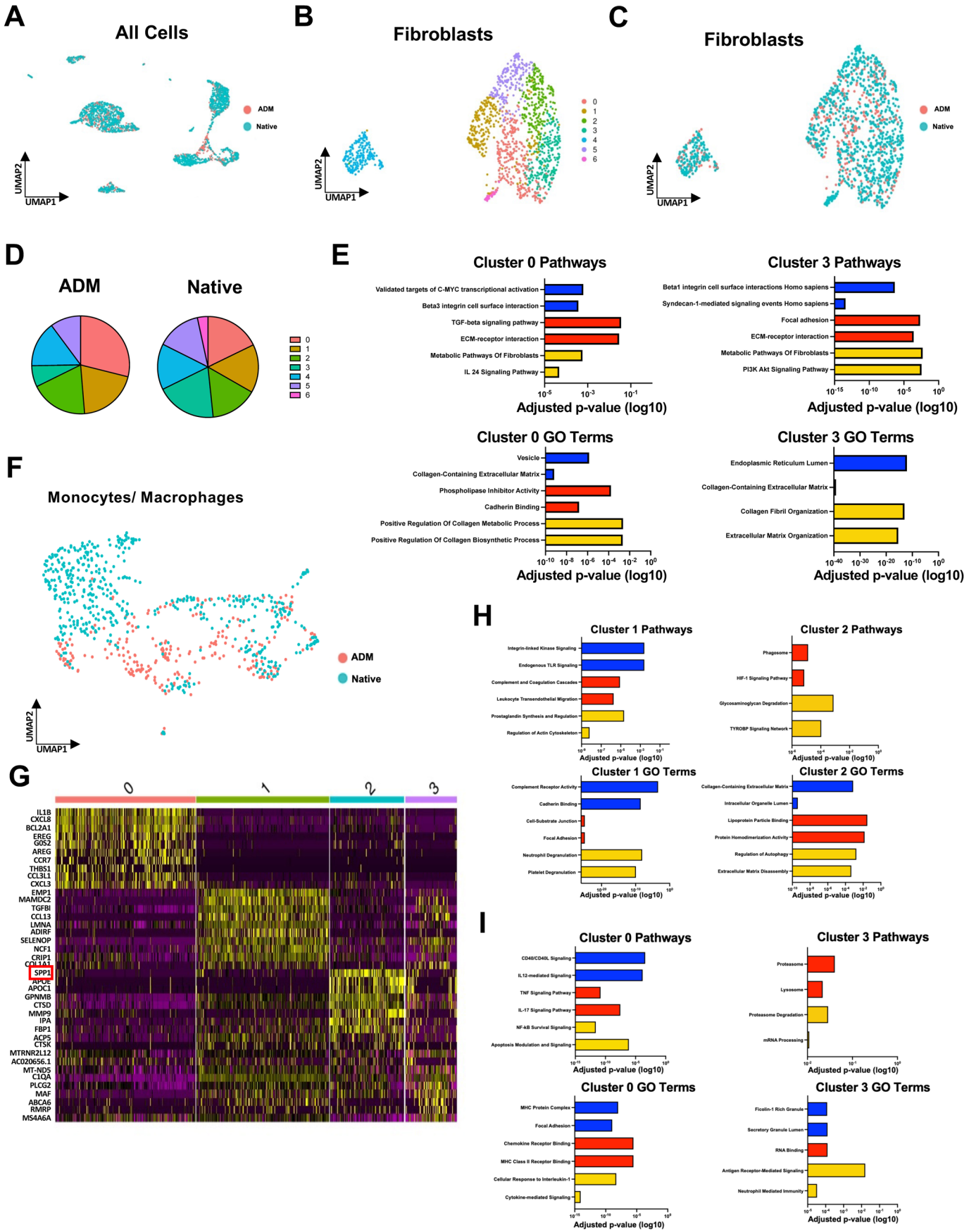

Extended Data Fig. 2 | See next page for caption.

https://doi.org/10.1038/s41551-025-01361-4

Extended Data Fig. 2 | scRNA-seq analysis of human capsule specimens with and without acellular dermal matrix (ADM). (**a**) Uniform-manifold approximation and projection (UMAP) of all cells colored by experimental condition [implant alone (Native) or Acellular Dermal Matrix-coated (ADM) capsule]. (**b**) UMAP of fibroblast cells (that is, *in silico* selection) colored by Seurat cluster (0–6). (**c**) UMAP of fibroblasts colored by experimental condition (Native or ADM capsule). (**d**) Relative representation of fibroblasts belonging to Seurat clusters 0–6 from ADM and Native capsules. (**e**) Enrichr analysis results for Pathways and Gene Ontology (GO) terms characteristic to cells in fibroblast Seurat clusters 0 and 3. (**f**) UMAP of myeloid cells colored by experimental condition (Native or ADM capsule). (**g**) Heatmap displaying top differentially expressed genes for each monocytes/macrophages Seurat cluster. The red square emphasizes that *SPP1* is a gene highly expressed in monocytes/macrophages Seurat cluster 2. (**h**) EnrichR analysis results for Pathways and Gene Ontology (GO) terms characteristic to cells in monocytes/macrophages cell Seurat clusters 1 and 2. (**i**) EnrichR analysis results for Pathways and Gene Ontology (GO) terms characteristic to cells in monocytes/macrophages Seurat clusters 0 and 3. Pathways: NCI-Nature 2016 (blue), KEGG 2021 Human (red), WikiPathway 2021 Human (yellow). GO Terms: GO Cellular Component 2021 (blue), GO Molecular Function 2021 (red), GO Biological Process (yellow).

https://doi.org/10.1038/s41551-025-01361-4

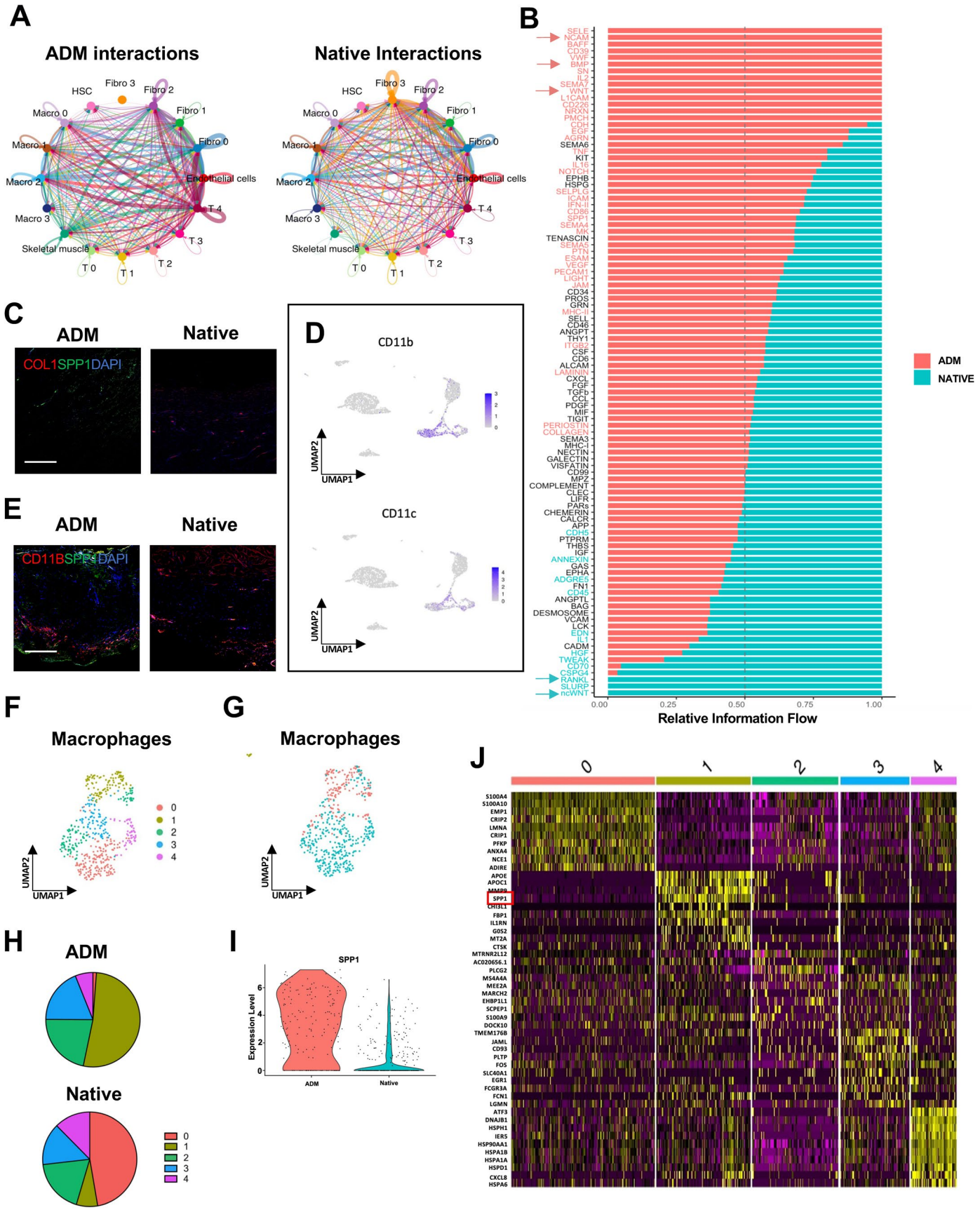

Extended Data Fig. 3 | See next page for caption.

https://doi.org/10.1038/s41551-025-01361-4

Extended Data Fig. 3 | Cell-cell interaction analysis of human capsule specimens with and without acellular dermal matrix (ADM). (**a**) Cell-cell interaction maps among cells from ADM capsule (left) and Native capsule (right). (**b**) Relative information flow for each significant pathway identified *via* CellChat. X-axis indicates the percentage of interactions per pathway identified in the dataset, split by experimental condition. Top signaling pathways colored in red are more enriched in ADM capsule, while those in green are more enriched in Native capsule. Red arrows highlight specific pathways enriched in ADM capsule, while green arrows highlight specific pathways enriched in Native capsule. (**c**) Immunofluorescence (IF) staining of Osteopontin (SPP1) (green signal) and Collagen Type 1 (COL1, green signal) in Native and ADM capsule. (**d**) All human cell single-cell RNA-sequencing Uniform-manifold approximation and projection (UMAP) colored by expression level for *Integrin Alpha M* (*CD11b*) (top) and *Integrin Alpha X* (*CD11c)* (bottom). (**e**) IF staining of SPP1 (green signal) and CD11b (red signal) in Native and ADM capsule. (**f**) Uniform-manifold approximation and projection (UMAPs) of macrophage cells colored by Seurat subcluster (0–4). (**g**) UMAP of macrophages colored by experimental condition (Native or ADM capsule). (**h**) Relative representation of macrophages belonging to Seurat subclusters 0–4 from ADM and Native capsule. (**i**) Violin plot displaying *Osteopontin* (*SPP1*) expression in macrophages by experimental condition (ADM or Native capsule). (**j**) Heatmap displaying top differentially expressed genes for each macrophage Seurat subcluster. The red square emphasizes that *SPP1* is a gene highly expressed in macrophage Seurat subcluster 1. (**c**, **e**) DAPI (4′,6-diamidino-2-phenylindole), nuclear counterstain (blue signal). Scale bars 100 μm.

https://doi.org/10.1038/s41551-025-01361-4

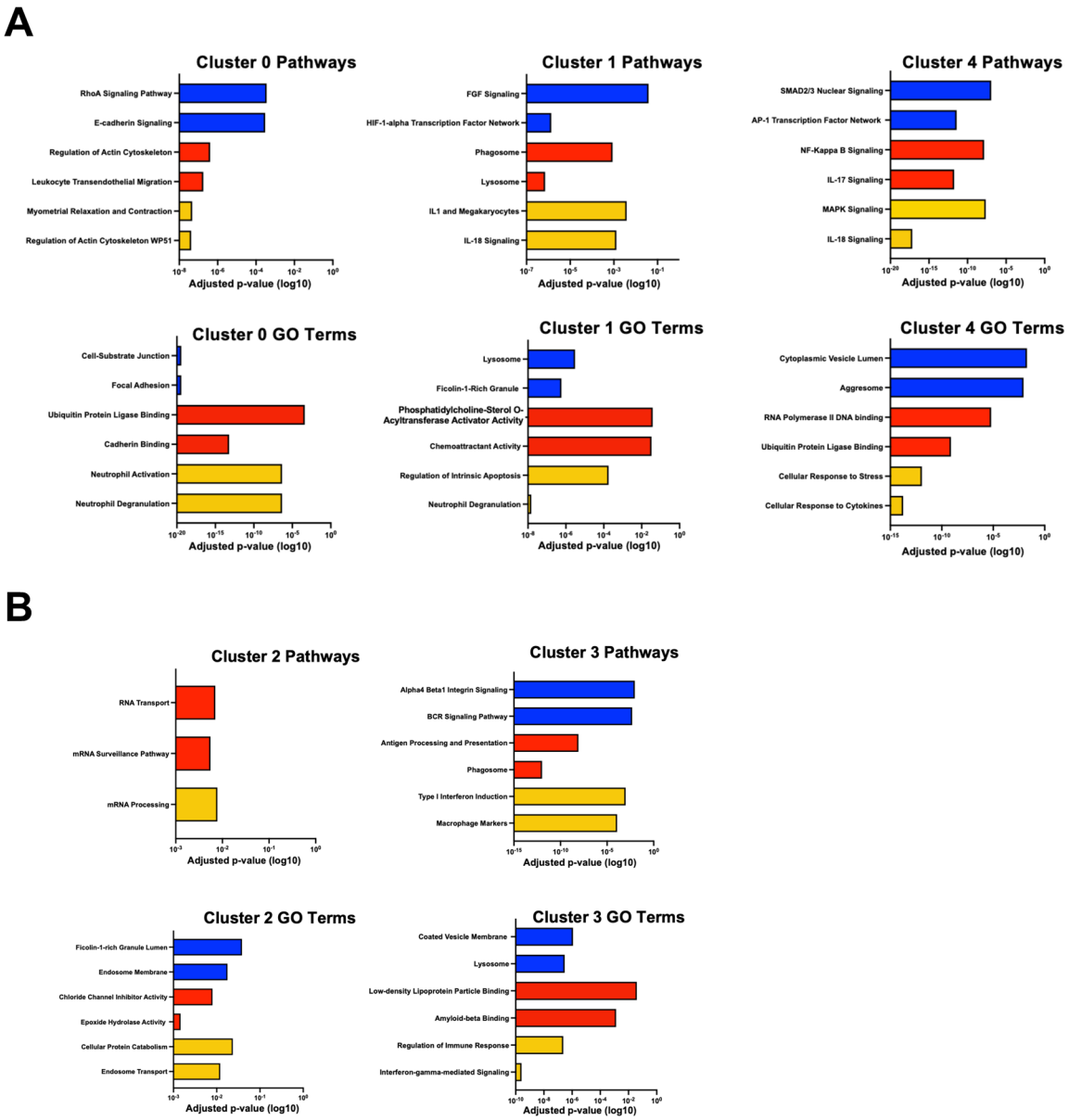

Extended Data Fig. 4 | See next page for caption.

https://doi.org/10.1038/s41551-025-01361-4

Extended Data Fig. 4 | Further scRNA-seq analysis of human capsule specimens with and without acellular dermal matrix (ADM), and comparison of native capsule to native capsule with no ADM exposure. (**a**) Enrichr analysis results for Pathways and Gene Ontology (GO) terms characteristic of cells in macrophage Seurat clusters 0, 1, and 4. (**b**) EnrichR analysis results for Pathways and Gene Ontology (GO) terms characteristic of cells in macrophage Seurat clusters 2 and 3. (**c**) Haematoxylin and eosin (H&E) staining of Native –ADM capsule. (**d**) Immunofluorescence (IF) staining of Osteopontin (SPP1) (green signal) and Integrin alpha X (CD11c) (red signal). (**e**) Quantification of SPP1 and CD11c co-expression from IF staining (n = 3 measurements from 3 separate biological replicates each of ADM, Native, and Native –ADM capsules, 9 total measurements). (**a**, **b**) Pathways: NCI-Nature 2016 (blue), KEGG 2021 Human (red), WikiPathway 2021 Human (yellow). GO Terms: GO Cellular Component 2021 (blue), GO Molecular Function 2021 (red), GO Biological Process (yellow). (**d**) DAPI (4′,6-diamidino-2-phenylindole), nuclear counterstain (blue signal). Data shown as mean ± standard deviation (S.D.); Statistical comparisons were made using an ordinary, one-way ANOVA, applying Bonferroni correction for multiple comparisons. DAPI (4′,6-diamidino-2-phenylindole), nuclear counterstain (blue signal). $^{****}P < 0.0001$, ns = not significant. Scale bars, (**c**) 400 μm; (**d**) 100 μm.

https://doi.org/10.1038/s41551-025-01361-4

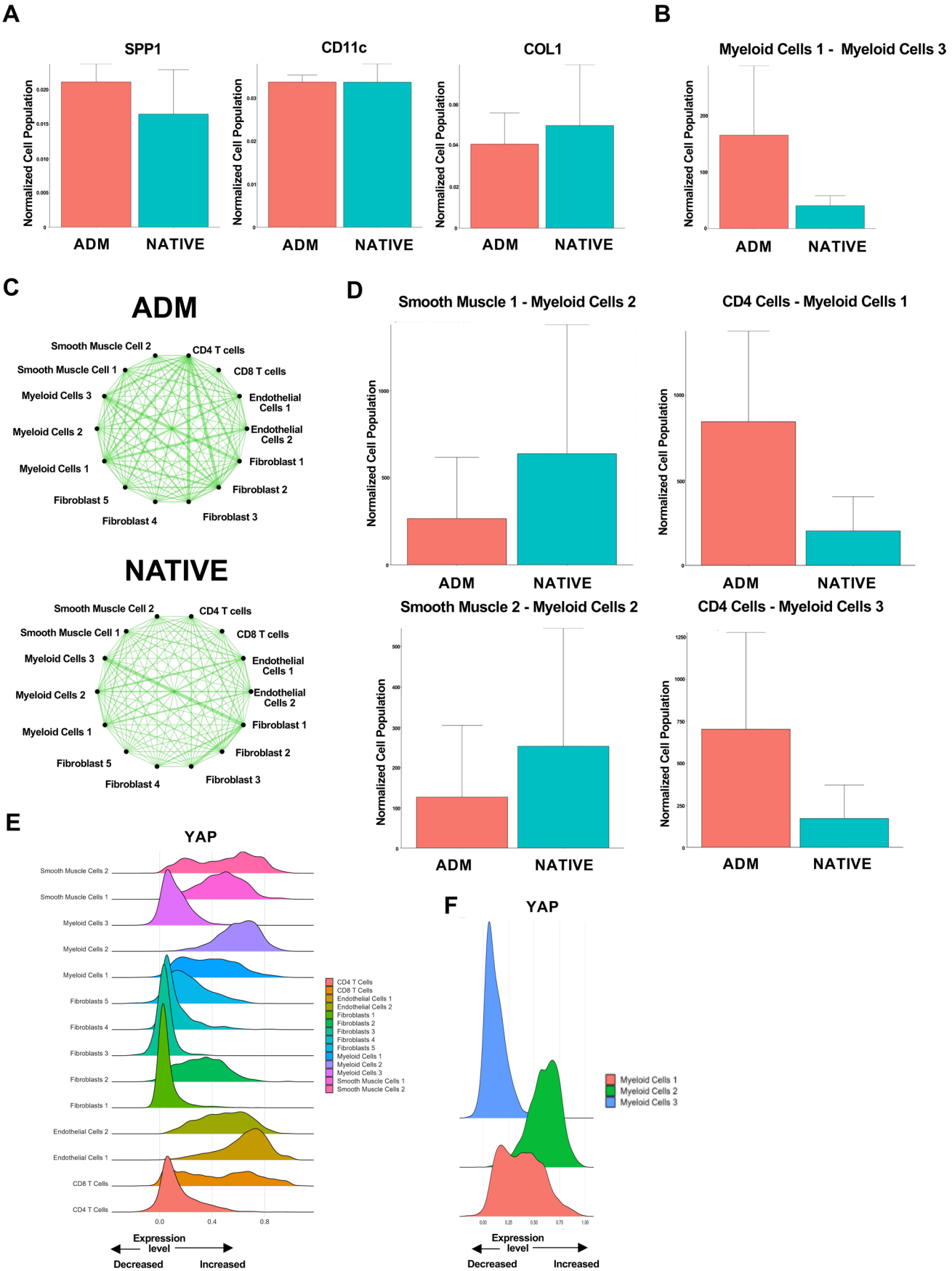

Extended Data Fig. 5 | See next page for caption.

https://doi.org/10.1038/s41551-025-01361-4

Extended Data Fig. 5 | Further CODEX analysis of human capsule specimens with and without acellular dermal matrix (ADM). (**a**) Bar graphs of Osteopontin (SPP1), Integrin Alpha M (CD11c), and Collagen Type 1 (COL1) protein expression in Acellular Dermal Matrix-coated (ADM) and implant alone (Native) capsules. (**b**) Bar graph quantifying Myeloid 1 and Myeloid 3 communication in ADM and Native capsules. (**c**) Differential interaction maps in ADM (top) and Native (bottom) capsules (**d**) Bar graph quantifying Smooth muscle cell and Myeloid cell communication in ADM and Native capsules (left, top and bottom). Bar graph quantifying cluster of differentiation 4 (CD4) cell and Myeloid cell communication in ADM and Native capsules (right, top and bottom). (**e**) Ridge plot showing Yes-associated protein (YAP) expression in all cells. (**f**) YAP expression in Myeloid clusters. Error bars represent mean ± standard deviation. n = 3 regions of interest each from ADM and Native capsules.

https://doi.org/10.1038/s41551-025-01361-4

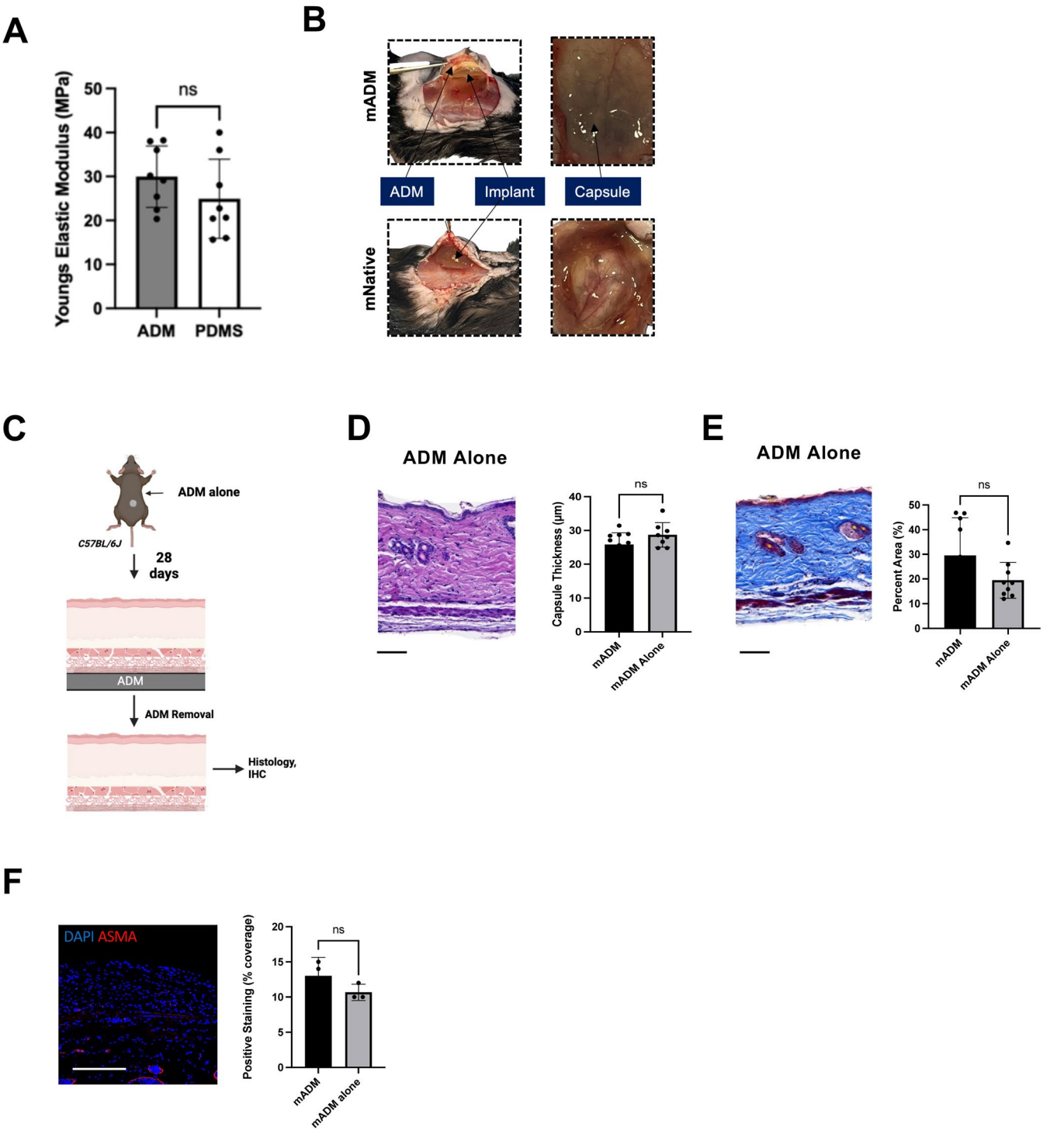

Extended Data Fig. 6 | Further mouse acellular dermal matrix (ADM) FBR model characterization. (**a**) Tensile Young's modulus of PDMS and ADM (n = 8 measurements from each material). (**b**) Gross photograph of mNative and mADM capsule retrieval (left). Photos on the right show magnified images of mNative and mADM capsules. (**c**) Schematic of experimental flow of the murine FBR model applied using ADM on its own. Implant and peri-implant tissue retrieved at postoperative day (POD) 28 for histology analysis. (**d**) Hematoxylin and eosin (H&E) staining of ADM alone capsule. Quantification of capsule thickness in mADM and ADM alone capsule (right) (n = 3 measurements from 3 separate biological replicates each of mADM and mADM alone capsules, 9 total measurements). (**e**) Trichrome staining of ADM alone capsule. Quantification of collagen density in mADM and ADM alone capsule (right) (n = 3 measurements from 3 separate biological replicates each of mADM and mADM alone capsules, 9 total measurements). (**f**) Immunofluorescence (IF) staining of α-Smooth Muscle Actin (α-SMA) (red signal) in ADM alone (far left). Quantification of α-SMA expression from IF staining (second panel from left) (n = 3 regions of interest from 3 separate biological replicates each of mADM and mNative capsules, 9 total measurements). (**f**) DAPI (4′,6-diamidino-2-phenylindole), nuclear counterstain (blue signal). Data shown as mean ± standard deviation (S.D.); statistical comparisons were made using an unpaired, two-tailed t-test. ns = not significant. Scale bars (**b**, **c**) 50 µm; (**d**) 100 µm. Created in BioRender. Parker, J. (2025) https://BioRender.com/t99s331.

https://doi.org/10.1038/s41551-025-01361-4

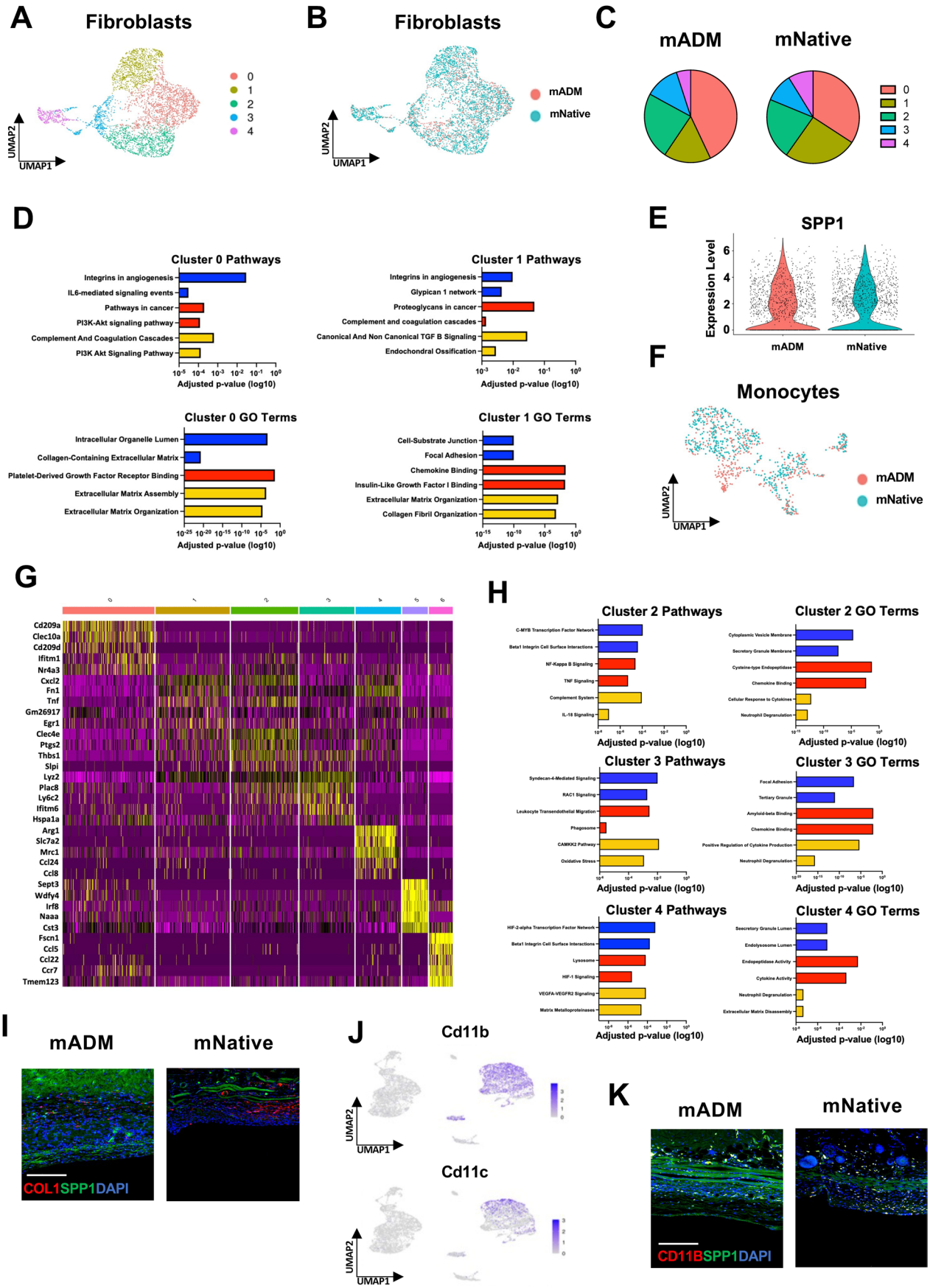

Extended Data Fig. 7 | See next page for caption.

https://doi.org/10.1038/s41551-025-01361-4

Extended Data Fig. 7 | scRNA-seq analysis of mouse capsules with and without acellular dermal matrix (ADM). (**a**) Uniform-manifold approximation and projection (UMAP) of fibroblasts colored by Seurat cluster (0–4). (**b**) UMAP of fibroblasts colored by experimental condition [Acellular Dermal Matrix-coated (mADM) or implant alone (mNative) capsule]. (**c**) Relative representation of fibroblasts belonging to fibroblast Seurat clusters 0–4 from mADM and mNative capsules. (**d**) EnrichR analysis results for Pathways and Gene Ontology (GO) terms characteristic to cells in fibroblast Seurat clusters 0 and 1. (**e**) Violin plot displaying *Osteopontin* (*SPP1*) expression in macrophages by experimental condition [Acellular Dermal Matrix-coated (mADM) or implant alone (mNative) capsule]. (**f**) UMAP of monocytes colored by experimental condition (mNative or mADM capsule). (**g**) Heatmap displaying top differentially expressed genes for each monocyte Seurat cluster. (**h**) EnrichR analysis results for Pathways and Gene Ontology (GO) terms characteristic of cells in monocyte Seurat clusters 2, 3, and 4. (**i**) Immunofluorescence (IF) staining of SPP1 (green signal) and Collagen Type I (COL1) (red signal) in mNative and mADM capsule. Bright green tissue is autofluorescence of panniculus carnosus. (**j**) All mouse single cell RNA-sequencing (scRNA-seq) UMAP colored by expression level for *Integrin alpha M* (*Cd11b*) (top) and *Integrin alpha X* (*Cd11c*) (bottom). (**k**) IF staining of SPP1 (green signal) and CD11b (red signal) in mNative and mADM capsule. Bright green tissue is autofluorescence of panniculus carnosus. (**i**, **k**) DAPI, nuclear counterstain (blue signal). Pathways: NCI-Nature 2016 (blue), KEGG 2021 Human (red), WikiPathway 2021 Human (yellow). GO Terms: GO Cellular Component 2021 (blue), GO Molecular Function 2021 (red), GO Biological Process (yellow). Scale bars = 100 μm.

https://doi.org/10.1038/s41551-025-01361-4

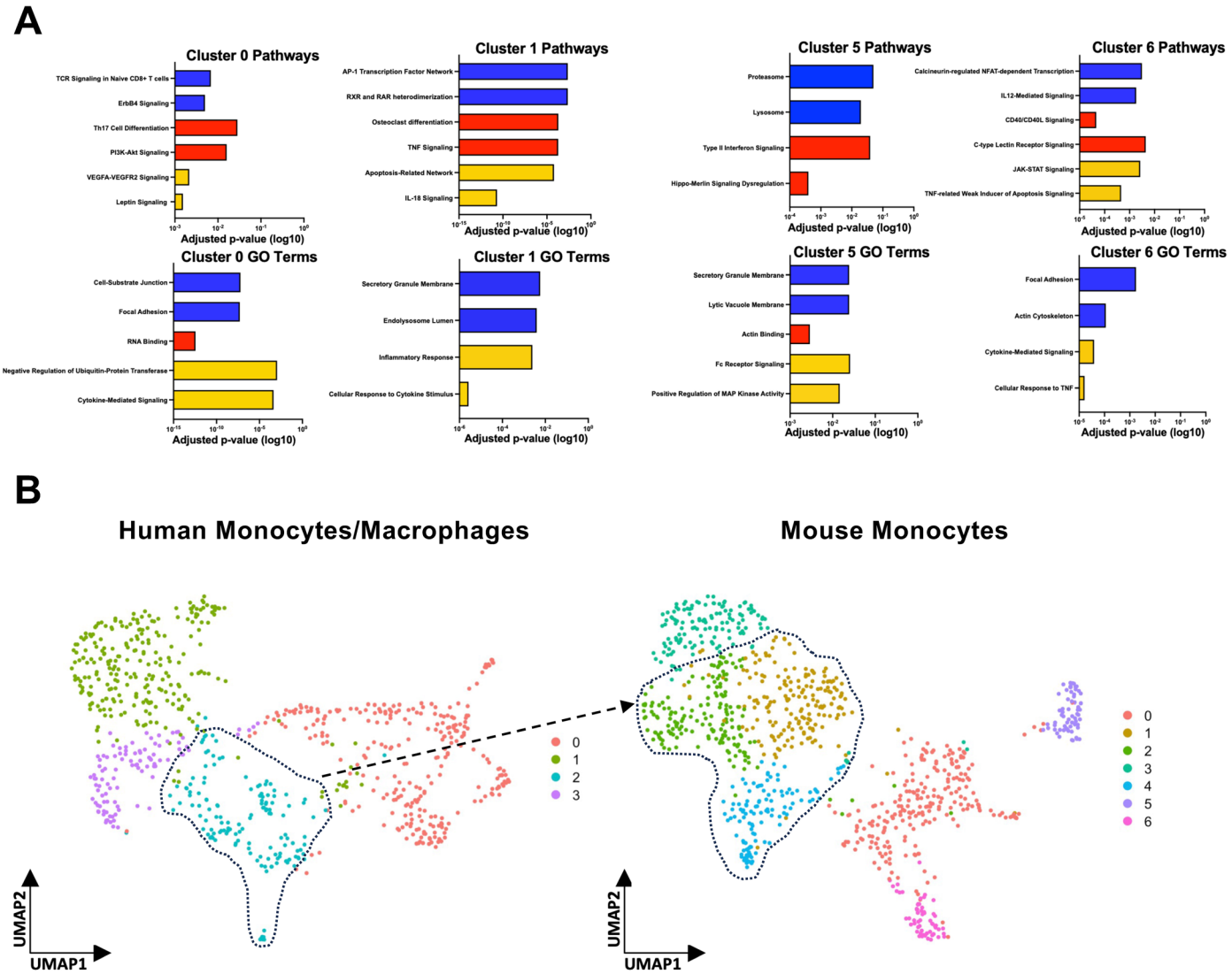

Extended Data Fig. 8 | Further scRNA-seq analysis of mouse capsules with and without acellular dermal matrix (ADM) and integration with human scRNA-seq data. (**a**) Enrichr analysis results for Pathways and Gene Ontology (GO) terms characteristic of cells in monocyte Seurat clusters 0, 1, 5, and 6. (**b**) Summary of correlations between human monocyte/macrophage cluster 2 from Fig. 2 to mouse monocyte clusters 1, 2, and 4 from Fig. 5. (**c**) Violin plot depitcting the similarity of human monocyte/macrophage cluster 2 onto mouse monocyte derived seurat clusters. Pathways: NCI-Nature 2016 (blue), KEGG 2021 Human (red), WikiPathway 2021 Human (yellow). GO Terms: GO Cellular Component 2021 (blue), GO Molecular Function 2021 (red), GO Biological Process (yellow).

https://doi.org/10.1038/s41551-025-01361-4

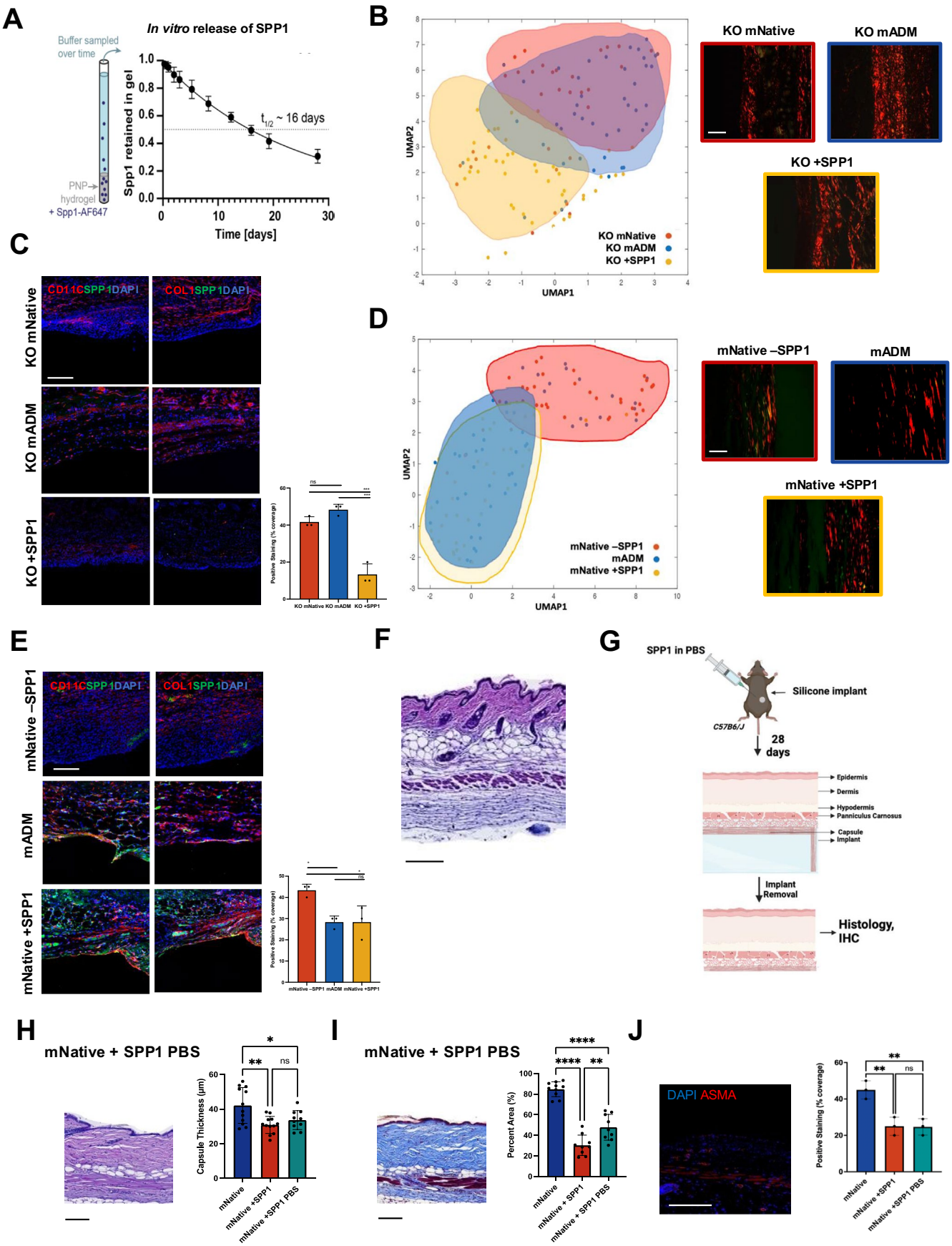

Extended Data Fig. 9 | See next page for caption.

https://doi.org/10.1038/s41551-025-01361-4

Extended Data Fig. 9 | SPP1 PNP hydrogel characterization and further histologic analysis of its application in vivo. (**a**) Schematic of Osteopontin-1 (SPP1) release from polymer-nanoparticle (PNP) hydrogel wherein 100 µL of PNP hydrogel with 15 µL of SPP1-AF647 is injected into the bottom of a capillary tube and PBS buffer added (left). Buffer is sampled over time to quantify SPP1 release. Quantification of release assay (right). (**b**) Picrosirius red histology (left) and uniform manifold approximation and projection (UMAP) displaying quantified extracellular matrix (ECM) ultrastructure parameters for KO mNative, KO mADM, and KO +SPP1 capsules (right), with capsule data displayed in red, blue, and yellow, respectively. (**c**) Immunofluorescence (IF) co-staining of Osteopontin-1 (SPP1) (green signal) and Integrin alpha X (CD11c) (red signal) (top) and co-staining of SPP1 (green signal) and Collagen Type I (COL1) (red signal) bottom in KO mNative, KO mADM, and KO +SPP1 capsules. Quantification of COL1 expression from IF staining (bottom) (n = 3 regions of interest from 3 separate biological replicates each of KO mNative, KO mADM, and KO +SPP1 capsules, 9 total measurements). (**d**) Picrosirius red histology (bottom) and uniform manifold approximation and projection (UMAP) displaying quantified extracellular matrix (ECM) ultrastructure parameters for mNative −SPP1, mADM, and mNative +SPP1 capsules (top), with capsule data displayed in red, blue, and yellow, respectively. (**e**) IF co-staining of SPP1 (green signal) and CD11c (red signal) (top) and co-staining of SPP1 (green signal) and COL1 (red signal) bottom in mNative −SPP1, mADM, and mNative +SPP1 capsules. Quantification of COL1 expression from IF staining (bottom) (n = 3 regions of interest from 3 separate biological replicates each of mNative −SPP1, mADM, and mNative +SPP1 capsules, 9 total measurements). (**f**) Hematoxylin and eosin (H&E) staining of mouse skin injected subcutaneously every other day with SPP1 resuspended in PBS. (**g**) Schematic of experimental flow of the murine FBR model used. Silicone implants combined with a subcutaneous injection of SPP1 in PBS (mNative + SPP1 PBS). Implant and peri-implant tissue retrieve at postoperative day (POD) 28 for histology analysis. (**h**) Hematoxylin and eosin (H&E) staining of mNative + SPP1 PBS capsule. Quantification of capsule thickness in mNative, mNative + SPP1, and mNative + SPP1 PBS capsule (right) (n = 3 measurements from 3 separate biological replicates each of mNative, mNative +SPP1, and mNative +SPP1 PBS capsules, 9 total measurements). (**i**) Trichrome staining of mNative + SPP1 PBS. Quantification of collagen density in mNative, mNative + SPP1, and mNative + SPP1 PBS capsule (right) (n = 3 measurements from 3 separate biological replicates each of mNative, mNative +SPP1, and mNative +SPP1 PBS capsules, 9 total measurements). (**j**) Immunofluorescence (IF) staining of α-Smooth Muscle Actin (α-SMA) (red signal) in mNative +SPP1 PBS (left). Quantification of α-SMA expression from IF staining (right) (n = 3 regions of interest from 3 separate biological replicates each of mNative, mNative +SPP1, and mNative +SPP1 PBS capsules, 9 total measurements). (**a**) Data are shown as mean ± SD and fit with a one-phase decay in GraphPad Prism and half-life of 16.11 days calculated. (**c**, **e**, **h**, **i**, **j**) Data shown as mean ± standard deviation (S.D.). Statistical comparisons were made using an ordinary, one-way ANOVA, applying Bonferroni correction for multiple comparisons. (**c**, **e**, **j**) DAPI (4′,6-diamidino-2-phenylindole), nuclear counterstain (blue signal). $^{*}P < 0.05$, $^{**}P < 0.01$, $^{***}P < 0.001$, $^{****}P < 0.0001$. (**b**, **d**) Scale bars 50 µm. (**c**, **e**, **j**) Scale bars 100 µm. n = 3 capsule specimens per condition unless otherwise specified. Created in BioRender. Parker, J. (2025) https://BioRender.com/e24s120.

https://doi.org/10.1038/s41551-025-01361-4

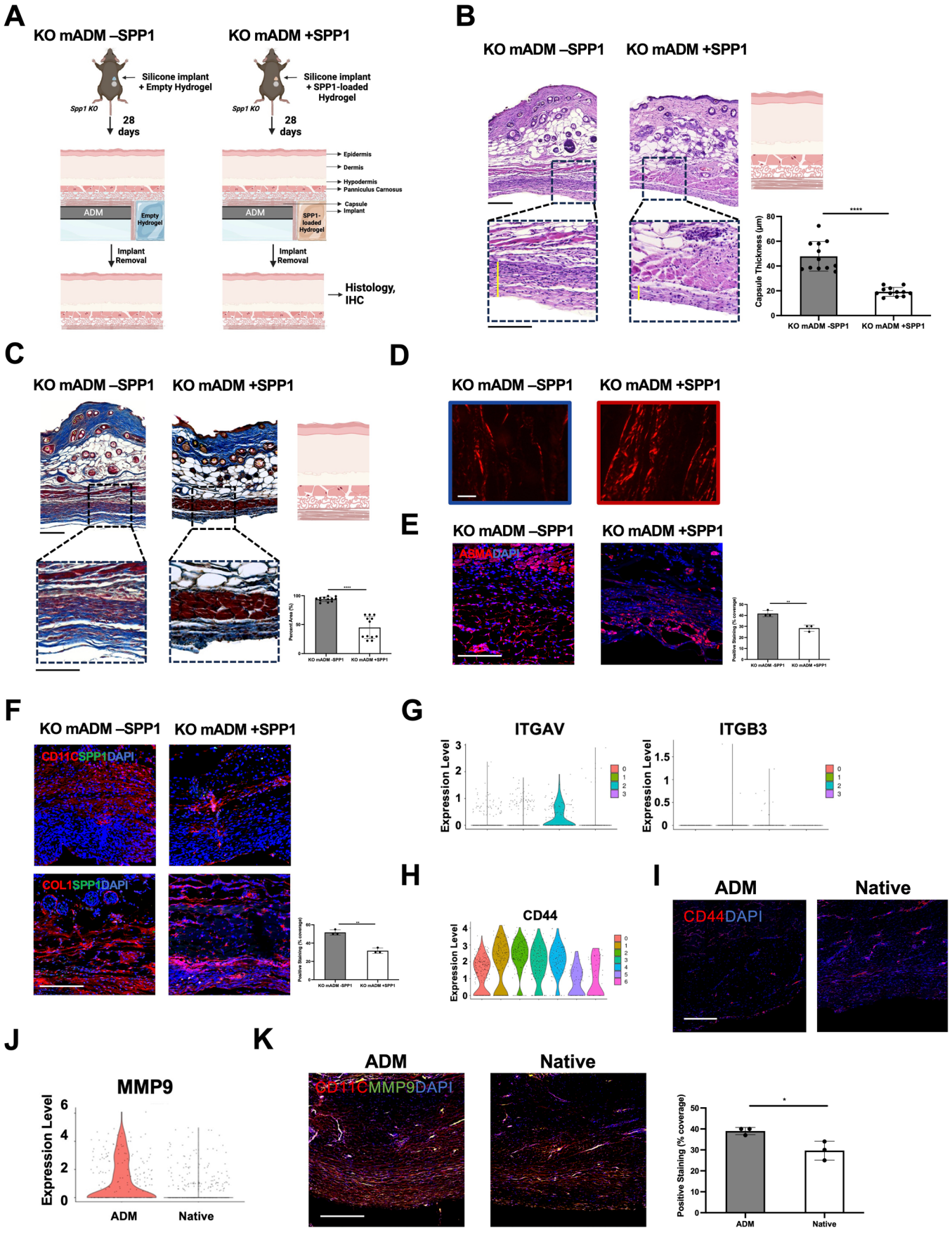

Extended Data Fig. 10 | See next page for caption.

https://doi.org/10.1038/s41551-025-01361-4

Extended Data Fig. 10 | Additional SPP1 KO groups and exploration into potential mechanistic pathways of SPP1 anti-fibrotic function. (**a**) Schematic of experimental flow of the murine FBR model used. Silicone implants coated with Acellular Dermal Matrix combined with an ipsilateral injection of empty PNP hydrogel (KO mADM −SPP1) and silicone implants coated with ADM combined with an ipsilateral injection of recombinant SPP1-loaded PNP hydrogel (KO mADM +SPP1) were implanted subcutaneously in the dorsi of *Spp1* Knock-Out (SPP1 KO) mice. Implant and peri-implant tissue retrieved at postoperative day (POD) 28 for histologic analyses. (**b**) Hematoxylin and eosin (H&E) staining of KO mADM −SPP1 (left) and KO mADM +SPP1 capsule (middle). Black dotted regions indicate areas from which magnified images were captured. Schematic representing skin layers and capsule (right, top). Yellow lines indicate capsule area. Quantification of capsule thickness in KO mADM −SPP1 and KO mADM +SPP1 capsule (right, bottom) (n = 4 measurements from 3 separate biological replicates each of KO mADM −SPP1 and KO mADM +SPP1, 12 total measurements). (**c**) Trichrome staining of KO mADM −SPP1 (left) and KO mADM +SPP1 capsules (middle). Black dotted regions indicate areas from which magnified images were captured. Schematic representing skin layers and capsule (right, top). Quantification of collagen density in KO mADM −SPP1 and KO mADM +SPP1 capsule (right, bottom) (n = 4 measurements from 3 separate biological replicates each of KO mADM −SPP1 and KO mADM +SPP1, 12 total measurements). (**d**) Picrosirius red histology of KO mADM −SPP1 and KO mADM +SPP1. (**e**) Immunofluorescence (IF) staining of alpha Smooth Muscle Actin (α-SMA) (red signal) in KO mADM −SPP1 and KO mADM +SPP1 (left and middle). Quantification of α-SMA expression from IF staining (bottom right) (n = 3 regions of interest from 3 separate biological replicates each of KO mADM −SPP1 and KO mADM +SPP1, 9 total measurements). (**f**) IF co-staining of Osteopontin-1 (SPP1) (green signal) and Integrin alpha M (CD11b) (top) and co-staining of SPP1 (green signal) and Collagen Type 1 (COL1) (red signal) (bottom) in KO mADM −SPP1 and KO mADM +SPP1 capsules. Quantification of COL1 expression from IF staining (bottom right) (n = 3 regions of interest from 3 separate biological replicates each of KO mADM −SPP1 and KO mADM +SPP1, 9 total measurements). (**g**) Violin plots displaying *Integrin Subunit Alpha V* (*ITGAV*) and *Integrin Subunit Beta 3* (*ITGB3*) expression in human monocytes/macrophages by Seurat cluster (0–6). (**h**) Violin plot displaying *Cluster of Differentiation 44* (*CD44*) expression in human monocytes/macrophages by Seurat cluster (0–6). (**i**) Immunofluorescence (IF) staining of CD44 (red signal) in ADM and Native capsule (left and right). (**j**) Violin plot displaying *Matrix Metallopeptidase 9* (*MMP9*) in human monocytes/macrophages by experimental condition (ADM or Native capsule). (**k**) IF co-staining of MMP9 (green signal) and Integrin Alpha M (CD11b) in ADM and Native capsules (left and middle). Quantification of MMP9 expression from IF staining (right) (n = 3 regions of interest from 3 separate biological replicates each of human ADM and Native capsules, 9 total measurements. (**b**, **c**, **e**, **f**, **k**) Data shown as mean ± standard deviation (S.D.); statistical comparisons were made using an unpaired, two-tailed t-test. ns = not significant. (**e**, **f**, **i**, **k**) DAPI (4′,6-diamidino-2-phenylindole), nuclear counterstain (blue signal). $^{*}P < 0.05$, $^{**}P < 0.01$, $^{****}P < 0.0001$. (**b**, **c**) Scale bars 50 µm; Scale bar insets 100 µm (**d**) Scale bars 50 µm. (**e**, **f**, **i**, **k**) Scale bars 100 µm. n = 3 unless otherwise specified. *Created in BioRender. Parker, J. (2025)* https://BioRender.com/q41e611.

nature portfolio

Corresponding author(s): Arash Momeni, Derrick Wan and Michael Longaker

Last updated by author(s): Jan 24, 2025

Reporting Summary

Nature Portfolio wishes to improve the reproducibility of the work that we publish. This form provides structure for consistency and transparency in reporting. For further information on Nature Portfolio policies, see our Editorial Policies and the Editorial Policy Checklist.

Statistics

For all statistical analyses, confirm that the following items are present in the figure legend, table legend, main text, or Methods section.

n/a	Confirmed
☐	☒ The exact sample size (*n*) for each experimental group/condition, given as a discrete number and unit of measurement
☐	☒ A statement on whether measurements were taken from distinct samples or whether the same sample was measured repeatedly
☐	☒ The statistical test(s) used AND whether they are one- or two-sided *Only common tests should be described solely by name; describe more complex techniques in the Methods section.*
☒	☐ A description of all covariates tested
☒	☐ A description of any assumptions or corrections, such as tests of normality and adjustment for multiple comparisons
☐	☒ A full description of the statistical parameters including central tendency (e.g. means) or other basic estimates (e.g. regression coefficient) AND variation (e.g. standard deviation) or associated estimates of uncertainty (e.g. confidence intervals)
☐	☒ For null hypothesis testing, the test statistic (e.g. *F*, *t*, *r*) with confidence intervals, effect sizes, degrees of freedom and *P* value noted *Give P values as exact values whenever suitable.*
☒	☐ For Bayesian analysis, information on the choice of priors and Markov chain Monte Carlo settings
☒	☐ For hierarchical and complex designs, identification of the appropriate level for tests and full reporting of outcomes
☒	☐ Estimates of effect sizes (e.g. Cohen's *d*, Pearson's *r*), indicating how they were calculated

Our web collection on statistics for biologists contains articles on many of the points above.

Software and code

Policy information about availability of computer code

Data collection	Human and mouse scRNA-seq libraries were sequenced on the Illumina platform, and data retrieved using CellRanger's mkfastq command to generate FASTQ files from BCL sequencing files.
Data analysis	The following R packages were used for downstream scRNA-seq analysis: Seurat (v.4.9), SingleR (v.2.2.0), CellChat (2.1.2). Monocle 3 (v. 1.3.6) and STvEA (v. 0.2.0) were used for spatial proteomic analysis. Prism Graphpad was used for statistical analyses. Matlab was used for ultrastructure analysis. Photoshop and ImageJ were used for other histological analyses.

For manuscripts utilizing custom algorithms or software that are central to the research but not yet described in published literature, software must be made available to editors and reviewers. We strongly encourage code deposition in a community repository (e.g. GitHub). See the Nature Portfolio guidelines for submitting code & software for further information.

Data

Policy information about availability of data

All manuscripts must include a data availability statement. This statement should provide the following information, where applicable:

- Accession codes, unique identifiers, or web links for publicly available datasets
- A description of any restrictions on data availability
- For clinical datasets or third party data, please ensure that the statement adheres to our policy

The scRNA-seq data generated during the study are available from the GEO repository (GSE: GSE279258). Original scripts for the ECM ultrastructure algorithm are

available from Github at https://github.com/shamikmascharak/Mascharak-et-al-ENF. The raw and analysed datasets generated during the study are available for research purposes from the corresponding authors on reasonable request.

Research involving human participants, their data, or biological material

Policy information about studies with human participants or human data. See also policy information about sex, gender (identity/presentation), and sexual orientation and race, ethnicity and racism.

Reporting on sex and gender	The patients were drawn from a population undergoing reconstructive breast surgery, a procedure for which the population at Stanford at the time of collection was 100% female. Although men were indirectly excluded from the study, these results may have broad implications applicable to both sexes.
Reporting on race, ethnicity, or other socially relevant groupings	These data were not recorded.
Population characteristics	Female adult patients (range 35 to 68 years). Specimens were obtained at time of implant procedure (range 3 to 24 months) following exapander placement.
Recruitment	Adult patients undergoing staged implant-based breast reconstruction either for prophylactic or therapeutic purposes. Specimens were obtained at time of implant procedure (range, 3 to 24 months) following expander placement. None of those patients had a history of post-op complications following expander or implant exchange.
Ethics oversight	Institutional Review Board at Stanford University.

Note that full information on the approval of the study protocol must also be provided in the manuscript.

Field-specific reporting

Please select the one below that is the best fit for your research. If you are not sure, read the appropriate sections before making your selection.

☒ Life sciences ☐ Behavioural & social sciences ☐ Ecological, evolutionary & environmental sciences

For a reference copy of the document with all sections, see nature.com/documents/nr-reporting-summary-flat.pdf

Life sciences study design

All studies must disclose on these points even when the disclosure is negative.

Sample size	Sample size was determined via Power analysis. In order to provide a power of 0.8 and to detect differences in the degree of fibrosis of 30% or greater between groups, we calculated that we needed 3 capsules minimum per time point per condition.
Data exclusions	All samples were included in the dataset.
Replication	All experiments were performed min n = 3, with all attempts at replication being successful.
Randomization	Human patients were not randomized, as the same procedure and tissue-collection method were performed on consecutive patients across the study time period. Mice were randomized between experimental and control groups.
Blinding	Human patients were not blinded, as the same procedure and tissue collection method were performed on consecutive patients across the study time period.

Reporting for specific materials, systems and methods

We require information from authors about some types of materials, experimental systems and methods used in many studies. Here, indicate whether each material, system or method listed is relevant to your study. If you are not sure if a list item applies to your research, read the appropriate section before selecting a response.

Materials & experimental systems

n/a	Involved in the study
☐	☒ Antibodies
☒	☐ Eukaryotic cell lines
☒	☐ Palaeontology and archaeology
☐	☒ Animals and other organisms
☒	☐ Clinical data
☒	☐ Dual use research of concern
☒	☐ Plants

Methods

n/a	Involved in the study
☒	☐ ChIP-seq
☒	☐ Flow cytometry
☒	☐ MRI-based neuroimaging

Antibodies

Antibodies used

Abeam ab216028 (anti-Integrin Alpha X; 1 1o 100), Abeam abS694 (anti-Alpha Smooth Muscle Actin; 1 to 200), ThermoFisher Scientific MAI-26771 (anti-Collagen Type I; 1 to 100), Abeam ab214050 (anti-Osteopontin; 1 to 100), ThermoFisher Scientific 14-0196-82 (anti-Integrin Alpha M; 1 to 100), ThermoFisher Scientific 14-0112-82 (anti-Integrin Alpha M; 1 to 100), ThermoFisher Scientific MAS-13890 (anti-Cluster of Differentiation 44; 1 to 100), ThermoFisher Scientific MAS-32705 (anti-Matrix Metallopeptidase 9; 1 to 100). Secondary antibodies include Alexa Fluor 488-conjugated anti-rabbit (Cat A11008; Lot: 2775963), anti-rat (Cat A21208; Lot 2482958), or anti-mouse (Cat A11029; Lot 2306579) antibodies (Invitrogen, Waltham, MA) and Alexa Fluor 594-conjugated anti-rabbit (Cat: A11037; Lot: 2841610), anti-rat (Cat A21209; Lot 2400917), or anti-mouse (Cat A11005; Lot 2641993) (Invitrogen, Waltham, MA). All secondaries were applied at a 1 to 200 dilution.

Validation

All antibodies were validated for immunohistochemistry by their respective manufacturer.
ab216028: recombinant fragment protein within Human ITGAX aa 600–850. Exact immunogen is proprietary; however, Abcam confirmed that the product has been tested on human paraffin-based IHC.
ab5694: synthetic peptide within Human ACTA2. Exact immunogen is proprietary; however, Abcam confirmed that the product has been tested on both human and mouse paraffin-based IHC.
ma1-26771: Invitrogen confirmed testing of the antibody in both frozen and FFPE specimens. Reactivity confirmed for mouse and human.
ab214050: Abcam confirmed that this antibody has been tested on human-based IF and IHC (paraffin).
14-0196-82: Invitrogen confirmed testing of the antibody on paraffin-based IHC in human tissue.
14-0112-82: Invitrogen confirmed testing of the antibody on paraffin-based IHC in mouse tissue.
ma5-13890: Invitrogen confirmed testing of the antibody on paraffin-based IHC in human tissue.
ma5-32705: Invitrogen confirmed testing of the antibody on paraffin-based IHC and IF in human tissue.

Animals and other research organisms

Policy information about studies involving animals; ARRIVE guidelines recommended for reporting animal research, and Sex and Gender in Research

Laboratory animals

Transgenic mouse strains (acquired from Jackson Laboratories): B6 (CS7BL/6J, Stock: 000664), Sppl (B6.129S6(Cg)-Sppltm1Blh/J, Stock: 004936). Mice were housed at the Stanford University Comparative Medicine Pavilion per Stanford APLAC guidelines, under the supervision of the Veterinary Service Center (VSC). Mice were all 8–12 weeks of age at the start of experiments.

Wild animals

The study did not involve wild animals.

Reporting on sex

Female and male mice were used for the animal studies.

Field-collected samples

The study did not involve samples collected from the field.

Ethics oversight

Administrative Panel on Laboratory Animal Care.

Note that full information on the approval of the study protocol must also be provided in the manuscript.